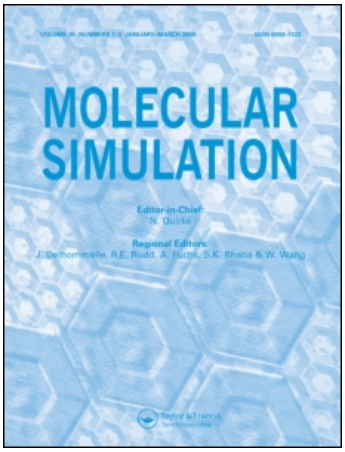

Molecular Simulation
Publication details, including instructions for authors and subscription information:
http://www.informaworld.com/smpp/title~content=t713644482

Grand Canonical Ensemble Monte Carlo Simulations of Ion Distribution Functions and of the Electric Double Layer in Spherical Charged or Uncharged Pores with Restricted Primitive Model 1:1 Electrolytes at Moderate Concentrations

Sergio Roberto Rivera[a]; Torben Smith Sørensen[b]
[a] Materials Science Group, Chemistry Department A, Blag. 207, Technical University of Denmark, Lyngby, Denmark [b] Institute of Physical Chemistry and Center for Modelling, Nonlinear Systems Dynamics and Irreversible Thermodynamics, Technical University of Denmark, Vanløse, Denmark

To cite this Article Rivera, Sergio Roberto and Sørensen, Torben Smith(1994) 'Grand Canonical Ensemble Monte Carlo Simulations of Ion Distribution Functions and of the Electric Double Layer in Spherical Charged or Uncharged Pores with Restricted Primitive Model 1:1 Electrolytes at Moderate Concentrations', Molecular Simulation, 14: 1, 35 — 66
To link to this Article: DOI: 10.1080/08927029408022006
URL: http://dx.doi.org/10.1080/08927029408022006

Molecular Simulation, 1994, Vol. 14, pp. 35–66
Reprints available directly from the publisher
Photocopying permitted by license only

GRAND CANONICAL ENSEMBLE MONTE CARLO SIMULATIONS OF ION DISTRIBUTION FUNCTIONS AND OF THE ELECTRIC DOUBLE LAYER IN SPHERICAL CHARGED OR UNCHARGED PORES WITH RESTRICTED PRIMITIVE MODEL 1:1 ELECTROLYTES AT MODERATE CONCENTRATIONS

SERGIO ROBERTO RIVERA[1] and TORBEN SMITH SØRENSEN[2]*

[1] *Materials Science Group, Chemistry Department A, Bldg. 207, Technical University of Denmark, DK2800 Lyngby, Denmark*

[2] *Institute of Physical Chemistry and Center for Modelling, Nonlinear Systems Dynamics and Irreversible Thermodynamics, Technical University of Denmark, Nørager Plads 3 DK2720 Vanløse, Denmark*

(Received June 1994, accepted June 1994)

A number of Grand Canonical Ensemble simulations have been performed for restricted primitive model 1:1 electrolytes in spherical hard-wall pores with the same dielectric permittivity in the pores and in the wall. The electrolyte concentrations are moderate corresponding to κa = ca. 0.9 and 1.4, where a = ionic diameter and κ is the inverse Debye length. The pores have a continuously distributed surface charge from 0 to 10 elementary charges and radii from 2 to 9 ionic diameters. Mean ionic distribution functions and the electric potential distributions in the spherical double layers are investigated. The mean ionic distribution functions seem to strike a balance between "attractive" hard sphere-hard wall effective forces and a repulsive force determined by the Debye length ($1/\kappa$) and due to the lack of symmetry in the ion clouds around ions near the wall. However, there is also in small pores a general depression of the mean ionic distribution functions, which increases with the applied external potential (wall charge). This electro-desorption phenomenon is contrary to the electro-sorption found earlier with dilute electrolyte solutions. Some few Debye lengths from the wall, bulk conditions prevail in the larger pores. The electric potential distributions may generally be expressed in terms of eigenfunctions of the Laplacian operator in analogy with the Debye-Hückel treatment. One or two eigen-functions are sufficient. In the case of two eigenfunctions, one may often fit the curves using eigenvalues λ^2, where one is close to κ^2 and the other λ is imaginary. For large pores it may be extremely difficult at the chosen electrolyte concentrations to determine the potential distribution except near to the wall without using runs of excessive lengths.

KEY WORDS: Spherical charged pores, primitive model electrolytes, ion and potential distributions, Grand Canonical Ensemble Monte Carlo, electro-desorption, Debye-Hückel eigenfunctions.

INTRODUCTION

In two previous paper [1,2], Grand Canonical Ensemble Monte Carlo (GCEMC) simulations of restricted primitive model electrolytes in small, spherical, charged or

* To whom all correspondence should be addressed.

non-charged pores were studied. The dielectric permittivities of the pores and of the pore walls were taken as identical. In reference 1, a preliminary study was made on population numbers, mean and single ion activity coefficients in pores, Donnan potentials as well as ion and electric potential distributions. More extensive studies were made in reference 2 focussing on quite dilute Z:Z electrolytes and on thermodynamic properties as spontaneous electrification of single pores and Donnan potentials of many pores in a "Swiss cheese" membrane model, which is quite relevant for many desalination membranes [3–7]. Also membrane activity coefficients and excess energies of the ions in the pores were investigated in reference 2.

In the present paper, two moderately concentrated restricted primitive model (RPM ~ same size of the ions) electrolytes are considered to be in equilibrium with various charged and uncharged spherical pores. We shall focus on the ion distribution functions and the electric potential distributions in the pores, since these distributions were not discussed in the previous paper. The model and the principles of the GCEMC calculations were carefully exposed in the previous papers [1, 2].

THE BASIC INPUT AND OUTPUT DATA

The input to the GCEMC programme consists of the following list of dimensionless parameters:

$$B(=\lambda_B/a);\ \rho^* = (a^3\rho_{tot});\ \mu_{\pm}(\text{ex})/kT(=\ln y_{\pm});\ Q/e_0;\ R/a(=\tau+0.5);\ \Delta \qquad (1)$$

B is the Bjerrum parameter (equal to the Bjerrum length divided by the ion diameter), ρ^* is the total ion concentration in the bulk solution with which the pore is in equilibrium (scaled by the ion diameter a), $\mu_{\pm}(\text{ex})/kT$ is the dimensionless mean ionic excess chemical potential (equal to the logarithm of the MacMillan-Mayer mean ionic activity coefficient $y_{\pm}$), Q/e_0 is the surface charge in elementary charge units, and R/a is the pore radius measured in ionic diameters (= the dimensionless accessible pore radius: $\tau + 1/2$). Finally, Δ is a dimensionless external electric potential difference applied to the pore relative to the bulk solution. This parameter was used in some simulations in references 1 and 2, for example as a Donnan potential to prevent spontaneous electrification of the pore. In the present paper, however, we have always put Δ equal to zero.

Instead of ρ^*, the concentration may also be measured as κa, where κ is the inverse Debye length, and

$$\kappa a = \sqrt{(4\pi B\rho^*)} \qquad (2)$$

The values of $\mu_{\pm}(\text{ex})/kT$ for the two concentrations used in this paper have been taken from the high precision hypernetted chain (integral equation) calculations performed in reference 8 for 1:1 electrolytes with $B = 1.681$. Some few simulations have been made with similar uncharged spherical particles at the higher of the two concentrations. The input value of $\mu(\text{ex})/kT$ in this case has been calculated using the "test particle" Canonical Ensemble MC programme described in earlier papers [4, 8–11] with the Bjerrum parameter chosen to be zero. The test particle value seems quite independent of the number of particles used and is equal to the value calculated by the Carnahan-Starling formula within the statistical uncertainty.

The basic output values from the GCEMC programme are the mean population numbers of the ions in the pores $\langle N_+ \rangle$ and $\langle N_- \rangle$, as well as the singlet distribution functions of the ions $G_p(t)$ and $G_m(t)$, which are functions of the dimensionless distance from the center

$$t = r/a \tag{3}$$

These distribution functions have been sampled in 90 equidistant shells in the pore as "local ion concentrations" divided by the salt concentration in the bulk solution $\rho_{tot}/2$. The values of the distribution functions are ascribed to the mid points of the spherical shells. To obtain better statistics-especially in the middle of the pore-the 90 shells may be compressed in adjacent pairs (to 45 values) or three and three (to 30 values). The price paid is then a greater discretisation error.

Table 1 surveys the simulations performed and the input parameters given. The simulation numbers with an asterisk correspond to the same numbers in reference 2, Table 1, but they have all been continued up to 60 millions of configurations (= successful or unsuccessful attempts to put and take ions in the pore, see reference 2, Appendix A). In a few cases (large pores) up to 240–480 millions of configurations have been used. This is required not to have too much "noise" in the distribution functions in the middle of the pores.

The values of $\langle N_+ \rangle$ and $\langle N_- \rangle$ are almost the same as stated before for a lower number of configurations, but for completeness, they are also listed in Table 2 of this paper together with the new variances VAR(N_+) and VAR(N_-). The variances are variances of the single configurational values, which explain their large values relative to the mean. The simulation numbers without an asterisk represent completely new simulations. In Table 2 we have also listed the mean excess energy of the ions in the pore and the variance of this quantity over the individual configurations.

THE MEAN IONIC DISTRIBUTION FUNCTIONS G_{pm}

Instead of $G_p(t)$ and $G_m(t)$, it is more adequate to calculate the two derived distributions $G_{pm}(t)$ and $\Delta G(t)$. The first is the *mean ionic distribution function* given by (for a Z:Z electrolyte)

$$G_{pm}(t) = \sqrt{\{G_p(t) \cdot G_m(t)\}} \tag{4}$$

The second is the dimensionless (and scaled) *local charge density* given by (for a 1:1 electrolyte)

$$\Delta G(t) = G_p(t) - G_m(t) \tag{5}$$

In this section we shall deal with $G_{pm}(t)$. In an ideal system, where the potential of mean forces for a specific ion in the pore may be separated into a "hard sphere contribution" and an electrostatic contribution, the mean ionic distribution function-but not $G_p(t)$ and $G_m(t)$ individually-should be unaffected by the wall charge, since the product of $\exp(-e_0\Psi/k_BT)$ and $\exp(+e_0\Psi/k_BT)$ makes unity. (The local electric potential is Ψ).

This separation is not correct in the moderately concentrated systems studied here, however, but still the process of taking the geometric mean removes a large part of the dependence on the wall charge.

We consider 1:1 electrolytes with $B = 1.681$, $\rho^* = 0.0393$ and $\rho^* = 0.09248$ corresponding to $\kappa a = 0.911141$ and 1.397669, respectively. Figures 1 and 2 show the function $G_{pm}(t)$ for pores with $R/a = 2$ and 5, respectively, for the bulk electrolyte in the lower of the two concentrations. The wall charge is 0, 5 and 10 elementary charges

Table 1 Survey of simulations performed.

$N°$	B	ρ^*	κa	$\mu_\pm(\text{ex})/kT$	Q/e_0	R/a	*no. of configurations* $\times 10^{-6}$
161*	1.681	0.03930	0.911141	−0.2590[a]	0	2.0	60
162*	1.681	0.03930	0.911141	−0.2590[a]	0	3.0	60
163*	1.681	0.03930	0.911141	−0.2590[a]	0	4.0	60
164*	1.681	0.03930	0.911141	−0.2590[a]	0	5.0	60
261	1.681	0.03930	0.911141	−0.2590[a]	1	7.0	480
262	1.681	0.03930	0.911141	−0.2590[a]	1	9.0	120
165*	1.681	0.03930	0.911141	−0.2590[a]	5	2.0	60
166*	1.681	0.03930	0.911141	−0.2590[a]	5	3.0	60
167*	1.681	0.03930	0.911141	−0.2590[a]	5	4.0	60
168*	1.681	0.03930	0.911141	−0.2590[a]	5	5.0	60
263	1.681	0.03930	0.911141	−0.2590[a]	5	7.0	240
264	1.681	0.03930	0.911141	−0.2590[a]	5	9.0	120
169*	1.681	0.03930	0.911141	−0.2590[a]	10	2.0	60
170*	1.681	0.03930	0.911141	−0.2590[a]	10	3.0	60
171*	1.681	0.03930	0.911141	−0.2590[a]	10	4.0	60
172*	1.681	0.03930	0.911141	−0.2590[a]	10	5.0	60
265	1.681	0.03930	0.911141	−0.2590[a]	10	7.0	240
266	1.681	0.03930	0.911141	−0.2590[a]	10	9.0	120
267	0	0.09248	–	0.4255[b]	–	2.0	60
268	0	0.09248	–	0.4255[b]	–	2.5	60
269	0	0.09248	–	0.4255[b]	–	3.0	60
270	0	0.09248	–	0.4255[b]	–	3.5	60
175*	1.681	0.09248	1.397669	−0.1240[a]	0	2.0	60
176*	1.681	0.09248	1.397669	−0.1240[a]	0	2.5	60
177*	1.681	0.09248	1.397669	−0.1240[a]	0	3.0	60
178*	1.681	0.09248	1.397669	−0.1240[a]	0	3.5	60
271	1.681	0.09248	1.397669	−0.1240[a]	1	5.0	240
272	1.681	0.09248	1.397669	−0.1240[a]	1	7.0	480
180*	1.681	0.09248	1.397669	−0.1240[a]	5	2.0	60
181*	1.681	0.09248	1.397669	−0.1240[a]	5	2.5	60
182*	1.681	0.09248	1.397669	−0.1240[a]	5	3.0	60
183*	1.681	0.09248	1.397669	−0.1240[a]	5	3.5	60
273	1.681	0.09248	1.397669	−0.1240[a]	5	5.0	120
274	1.681	0.09248	1.397669	−0.1240[a]	5	7.0	240
185*	1.681	0.09248	1.397669	−0.1240[a]	10	2.0	60
186*	1.681	0.09248	1.397669	−0.1240[a]	10	2.5	60
187*	1.681	0.09248	1.397669	−0.1240[a]	10	3.0	60
188*	1.681	0.09248	1.397669	−0.1240[a]	10	3.5	60
275	1.681	0.09248	1.397669	−0.1240[a]	10	5.0	120
276	1.681	0.09248	1.397669	−0.1240[a]	10	7.0	240

* Simulations numbers with asterisk are continuations of simulations with the same numbers in reference 2.
[a] From the HNC calculation in reference 8.
[b] Carnahan-starling (Compressibility): 0.42548. Percus-Yevick (Compressibility): 0.42566. CEMC (test particle) N = 120, 15 mill.: 0.4252. N = 62, 18 mill.: 0.4260. N = 32, 12 mill.: 0.4270.

Table 2 Simulated thermodynamic variables with their respective variances.

$N°$	$\langle N_+ \rangle$	$VAR\langle N_+ \rangle$	$\langle N_- \rangle$	$VAR\langle N_- \rangle$	$\langle U/kT \rangle$	$VAR(\langle U/kT \rangle)$
161	2.32584e − 1	2.00143e − 1	2.33022e − 1	2.00580e − 1	− 8.41606e − 2	1.18383e − 1
162	1.18095e + 0	8.21971e − 1	1.18023e + 0	8.21884e − 1	− 7.08943e − 1	8.42871e − 1
163	3.35039e + 0	2.03849e + 0	3.34919e + 0	2.03726e + 0	− 2.32490e + 0	2.54523e + 0
164	7.22452e + 0	4.08298e + 0	7.22527e + 0	4.08480e + 0	− 5.33702e + 0	5.66472e + 0
261	2.16884e + 1	1.15370e + 1	2.24755e + 1	1.16215e + 1	− 1.73733e + 1	1.79237e + 1
262	4.92750e + 1	2.52037e + 1	5.01089e + 1	2.52747e + 1	− 3.99988e + 1	4.09999e + 1
165	2.16098e − 2	2.13404e − 2	1.99985e + 0	6.14372e − 1	− 7.11081e + 0	4.83869e + 0
166	4.61829e − 1	4.10649e − 1	3.09108e + 0	1.16801e + 0	− 6.17182e + 0	2.77491e + 0
167	2.15778e + 0	1.61366e + 0	5.30604e + 0	2.31270e + 0	− 6.72855e + 0	3.48612e + 0
168	5.72621e + 0	3.72499e + 0	9.23207e + 0	4.31542e + 0	− 9.00544e + 0	6.24588e + 0
263	2.02438e + 1	1.13241e + 1	2.41737e + 1	1.17499e + 1	− 1.99982e + 1	1.81508e + 1
264	4.76694e + 1	2.50672e + 1	5.18384e + 1	2.54055e + 1	− 4.20520e + 1	4.10253e + 1
169	3.44271e − 3	3.43493e − 3	4.79687e + 0	7.05236e − 1	− 3.12326e + 1	1.37497e + 1
170	2.34965e − 1	2.21523e − 1	5.93614e + 0	1.28449e + 0	− 2.33622e + 1	7.49691e + 0
171	1.50456e + 0	1.24225e + 0	7.96279e + 0	2.40872e + 0	− 2.01433e + 1	6.15987e + 0
172	4.65218e + 0	3.32589e + 0	1.17196e + 1	4.41226e + 0	− 2.00478e + 1	7.92179e + 0
265	1.86540e + 0	1.10450e + 1	2.65251e + 1	1.18802e + 1	− 2.81954e + 1	1.90348e + 1
266	4.58326e + 1	2.48243e + 1	5.41735e + 1	2.54967e + 1	− 4.85960e + 1	4.16292e + 1
267	7.45898e − 1	6.58378e − 1	7.44495e − 1	6.56124e − 1	–	–
268	1.71035e + 0	1.49217e + 0	1.71111e + 0	1.49203e + 0	–	–
269	3.27943e + 0	2.84371e + 0	3.27674e + 0	2.83980e + 0	–	–
270	5.59077e + 0	4.81833e + 0	5.59226e + 0	4.82481e + 0	–	–
175	6.22632e − 1	4.28495e − 1	6.22775e − 1	4.28480e − 1	− 4.05021e − 1	5.04938e − 1
176	1.52085e + 0	8.81354e − 1	1.52108e + 0	8.81844e − 1	− 1.21230e + 0	1.33627e + 0
177	3.00362e + 0	1.56461e + 0	3.00365e + 0	1.56484e + 0	− 2.21879e + 0	2.72420e + 0
178	5.21417e + 0	2.53624e + 0	5.21497e + 0	2.53656e + 0	− 4.78129e + 0	4.83288e + 0
271	1.72995e + 1	7.67313e + 0	1.80922e + 1	7.74239e + 0	− 1.75835e + 1	1.69596e + 1
272	5.29429e + 1	2.20055e + 1	5.37929e + 1	2.20584e + 1	− 5.46950e + 1	5.22232e + 1
180	9.47755e − 2	8.96596e − 2	2.66158e + 0	6.73592e − 1	− 8.66137e + 0	3.54381e + 0
181	5.91221e − 1	4.78019e − 1	3.56889e + 0	1.08081e + 0	− 8.17339e + 0	3.03000e + 0
182	1.76108e + 0	1.19270e + 0	5.04818e + 0	1.74481e + 0	− 8.60474e + 0	3.85596e + 0
183	3.75501e + 0	2.21390e + 0	7.27715e + 0	2.70223e + 0	− 1.00407e + 1	5.66780e + 0
273	1.58600e + 1	7.50342e + 0	1.98225e + 1	7.85240e + 0	− 2.12722e + 1	1.73643e + 1
274	5.13246e + 1	2.18740e + 1	5.55803e + 1	2.21231e + 1	− 5.74124e + 1	5.24818e + 1
185	1.63635e − 2	1.61882e − 2	5.50528e + 0	7.16080e − 1	− 3.40208e + 1	1.03704e + 1
186	2.58098e − 1	2.32500e − 1	6.43005e + 0	1.09478e + 0	− 2.93659e + 1	7.44881e + 0
187	1.10101e + 0	8.46060e − 1	7.78992e + 0	1.74443e + 0	− 2.67191e + 1	7.01309e + 0
188	2.78849e + 0	1.84588e + 0	9.89190e + 0	2.71198e + 0	− 2.58638e + 1	8.04504e + 0
275	1.43001e + 1	7.22226e + 0	2.22320e + 1	7.89980e + 0	− 3.27682e + 1	1.85743e + 1
276	4.94070e + 1	2.17200e + 1	5.79250e + 1	2.22111e + 1	− 6.58511e + 1	5.32700e + 1

(uniformly distributed). Looking first at Figure 2 (the larger pore), we observe that with regard to $G_{pm}(t)$ bulk properties prevail in a surprisingly large central part of the pore (up to at least $t \approx 2$). In this part, $G_{pm}(t) = 1$ within the statistical "noise". Near the wall, however, there is a general depression of the curve exhibiting a minimum and a slight increase very near the wall.

There is no significant difference between zero wall charge and $Q/e_0 = 5$. Increasing the wall charge to 10, however, a very slight depression of the minimum is observed. This is well in accordance with the findings in reference 1, where no difference could be seen between $Q/e_0 = 0$ and $Q/e_0 = 1$ for the same electrolyte solution.

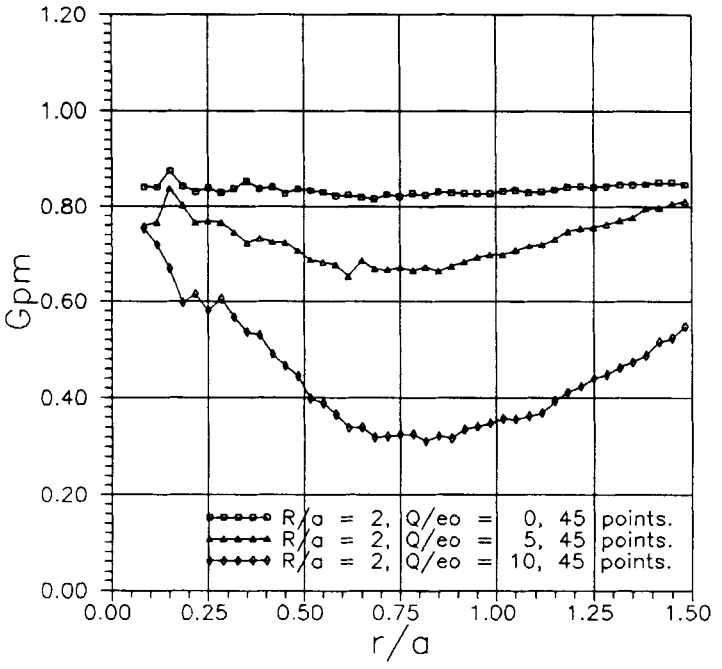

Figure 1 The mean ionic distribution function G_{pm} as a function of $t = r/a$ in spherical pores with a radius equal to two times the ionic diameter ($R/a = 2$). The continuously distributed surface charge of the pore is 0, 5 and 10 elementary charges. Increasing charge results in increasing electro-desorption (depression of the curves). The number of ions were sampled in 90 shells, which were contracted to 45 shells. $B = 1.681$, $\rho^* = 0.0393$.

The natural explanation for the observed phenomena is the following: When the ions approach the wall to within one Debye length, it is not possible to form a symmetric ionic cloud around the ion and the "local free energy" of the ion becomes higher, so that the local mean ionic occupation number decreases. The (dimensionless) Debye length is $1/\kappa a \approx 1.1$, and if the last upward bend is neglected, it is seen that the depression is roughly exponential from the wall contact ($t = 4.5$) and towards the interior with around this decay length. The upward bent is explained as effective "hard sphere/hard wall attractive forces". With an ion more and more close to wall contact, it is increasingly difficult for other ions to be between the ion and the wall. The average force will therefore tend to squeeze the ion against the wall and the local mean ionic concentration of ions increases very near the wall.

The same features are seen in the smaller pore with $R/a = 2$, Figure 1. Now the Debye length is only slightly smaller than the radius of the accessible part of the pore ($\tau = 1.5$), however, and there is no part of the pore with bulk properties. There is a general depression in the whole pore. Nevertheless, in the middle of the pore, the values of G_{pm} tend to the same value (≈ 0.8) for the three wall charges 0, 5 and 10. The minima of all three curves are now clearly shifted towards lower values for higher wall charges. In contrast to the *electro-sorption* found in references 1 and 2 for *dilute* systems when the total applied potential (the ion free potential from the wall $+\Delta$) was increased, we seem

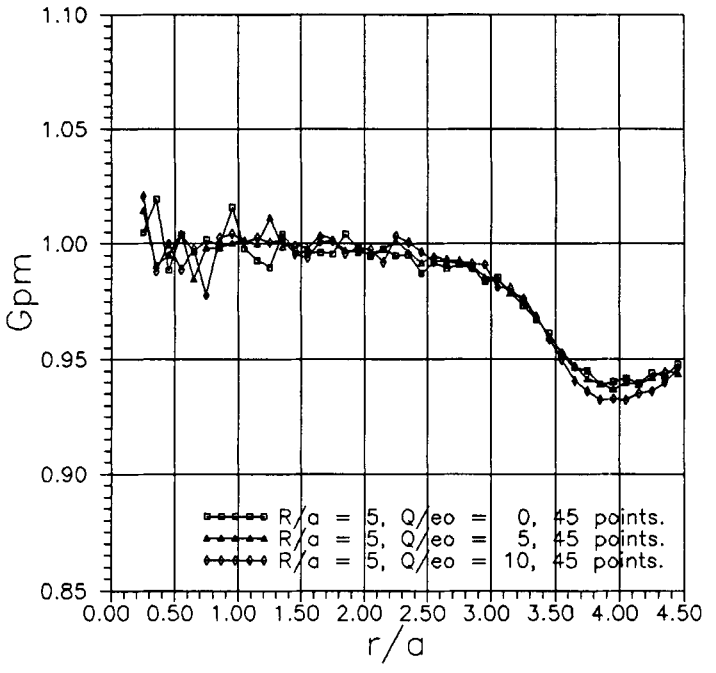

Figure 2 G_{pm} as a function of $t = r/a$ for a pore with $R/a = 5$. There is a large central part with bulk properties ($G_{pm} \approx 1$). The "noise" for small r/a is due to the small volume of the central shells. The mean ion is repelled by the wall, because the formation of a symmetric ionic cloud is prevented. Very near to the wall G_{pm} again increases somewhat due to the "hard sphere/hard wall effective attraction". $B = 1.681$, $\rho^* = 0.0393$.

to have *electro-desorption* in this moderately concentrated electrolyte – most pronounced in the smallest pores. The reason is probably, that space restrictions are very much felt, when the negative counter-ions crowd up in the pore at high positive wall charges.

In Figure 3, the mean ionic distribution functions in chargeless pores with $R/a = 2, 3, 4$ and 5 are shown. The bulk concentration is again $\rho^* = 0.0393$. The pores with $R/a = 4$ and 5 have clearly a central part with bulk properties, whereas the pore with $R/a = 2$ has clearly not. All curves exhibit the characteristic minimum, which is displaced towards lower values for the smaller pores. The same features are shown for wall charges 5 and 10 (Figures 4 and 5), but the minima are displaced towards lower values at higher values of Q/e_0 (electro-desorption)-especially in the case of the smallest pores.

If we now pass to $B = 1.681$ and the higher concentration $\rho^* = 0.09248$, we observe for $R/a = 3.5$ (Figure 7) the same pattern as before with the difference, that the "hard sphere/hard wall attractive forces" are stronger, because of the higher concentration. Bulk properties prevail up to $t \approx 1.5$ for all wall charges up to 10. There is a pronounced electro-desorption even for $Q/e_0 = 5$. For $R/a = 2$ (Figure 6), the picture is very similar to Figure 1 (with the lower concentration). Indeed, the curves for $Q/e_0 = 5$ and 10 seem almost indistinguishable for the two concentrations, whereas the curve for $Q/e_0 = 0$ is somewhat *more* depressed at the *lower* concentration. This might be so, because the Debye length is shorter at the higher concentration (less depression) and that

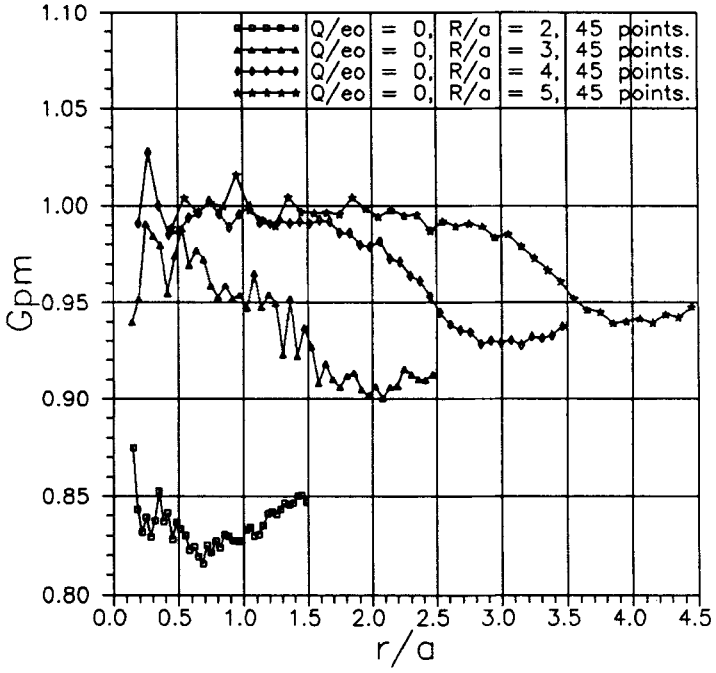

Figure 3 G_{pm} for chargeless pores with $R/a = 2, 3, 4$ and 5. There can be no electro-desorption here, so the increasing depression of the curves with decreasing radii must be caused by the ionic cloud asymmetry repulsion from the wall. The smallest pore is completely dominated by surface effects. $B = 1.681$, $\rho^* = 0.0393$.

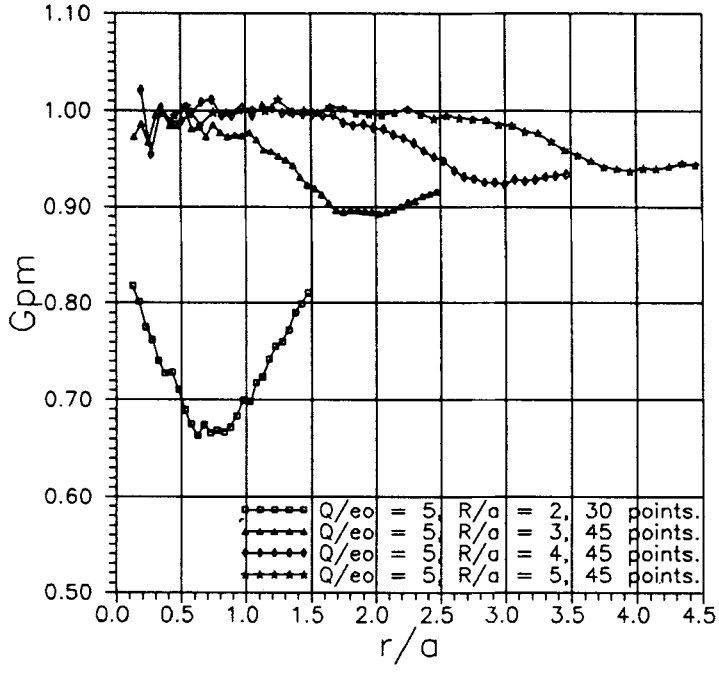

Figure 4 The same as Figure 3, but with a surface charge equal to 5 units. Electro-desorption is visible for the smallest pore when compared to Figure 3. $B = 1.681$, $\rho^* = 0.0393$.

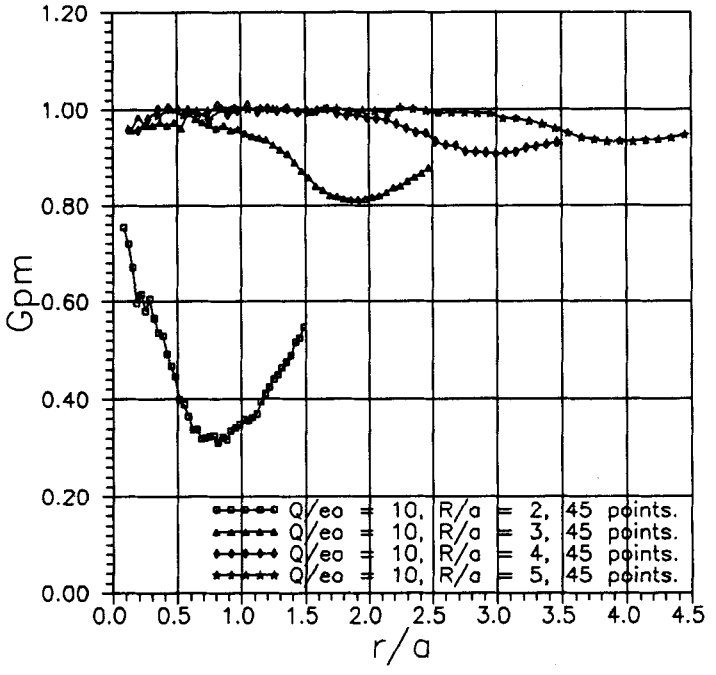

Figure 5 The same as Figure 3, but with a surface charge equal to 10 units. Electro-desorption is visible for the two smallest pores when compared to Figures 3 and 4. $B = 1.681$, $\rho^* = 0.0393$.

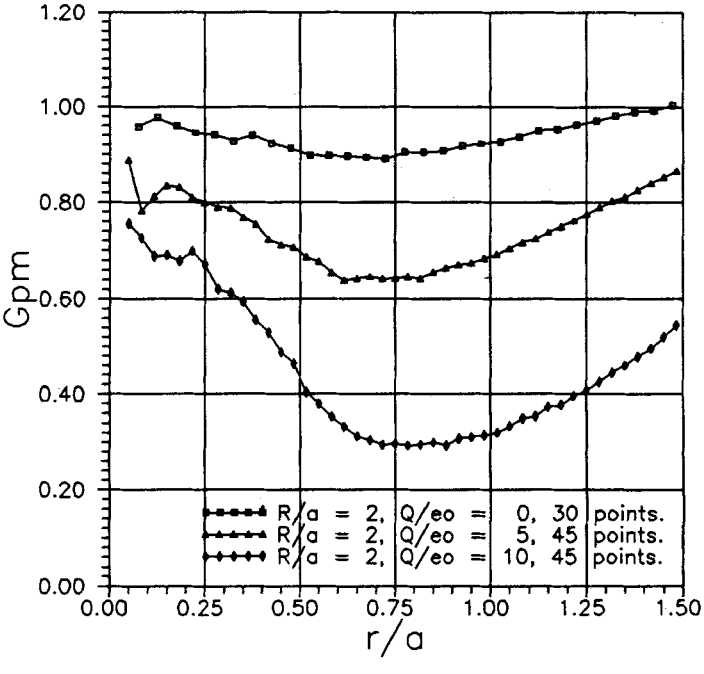

Figure 6 The same as Figure 1, but at a higher electrolyte concentration. Comparing to Figure 1 it is seen, that the curves for $Q/e_0 = 0$ and 5 are independent of the concentration, but for chargeless pores the low concentration exhibits a greater depression for the low concentration than for the high. $B = 1.681$, $\rho^* = 0.09248$.

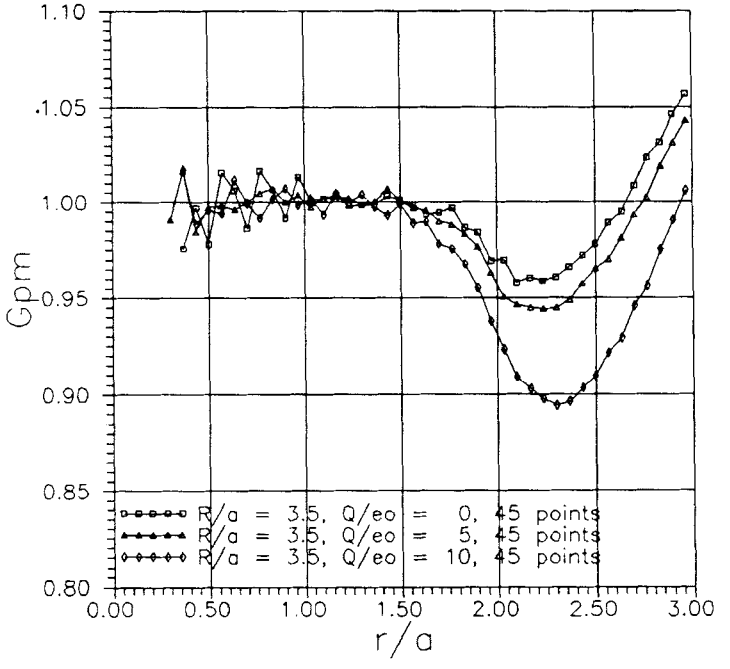

Figure 7 G_{pm} as a function of $t = r/a$ for a pore with $R/a = 3.5$. Electro-desorption is clearly visible in the surface region dominated by "asymmetric ionic cloud repulsion" and "hard sphere/hard wall attraction". $B = 1.681$, $\rho^* = 0.09248$.

simultaneously the upward bend (sphere/wall interactions) is more pronounced. However, this explanation cannot be valid at $Q/e_0 = 5$ and 10. In other words, the electro-desorption is *more* pronounced for low wall charges (from $Q/e_0 = 0$ to 5) at the *higher* concentration (more space restrictions for counter ion crowding), whereas the effect is the same from $Q/e_0 = 5$ to 10. This is well in line with the earlier findings, that there is electro-sorption and not desorption at dilute conditions.

Figures 8–10 show $G_{pm}(t)$ for pores with radii $R/a = 2$, 2.5, 3.0 and 3.5 at the high concentration with $Q/e_0 = 0$, 5 and 10, respectively. Compared to Figures 3–5 at the lower concentration, the hard sphere effects near the wall are much more pronounced. There is a clear electro-desorption.

Figure 11 shows the $G_{pm}(t)$ for a pore with $R/a = 7$ and 9 at the low concentration for $Q/e_0 = 1$, 5 and 10. The wall charge seems to be without significance. There is a wide central "bulk region" and a narrow surface region exhibiting ion cloud/wall repulsion as well as hard sphere/wall "attraction". In Figure 12, the same is observed for the high concentration and $R/a = 5$ and 7, where the surface region is even more narrow, and the hard sphere/wall "attraction" more dominant.

In Figure 13, results for G_{pm} are shown for $B = 0$, $\rho^* = 0.09248$ and $R/a = 2$, 2.5, 3 and 3.5. This correspond to chargeless particles of the same size, and $G_p = G_m = G_{pm}$. The wall charge is immaterial. The input excess chemical potentials are taken to be the values calculated from the Carnahan-Starling expression

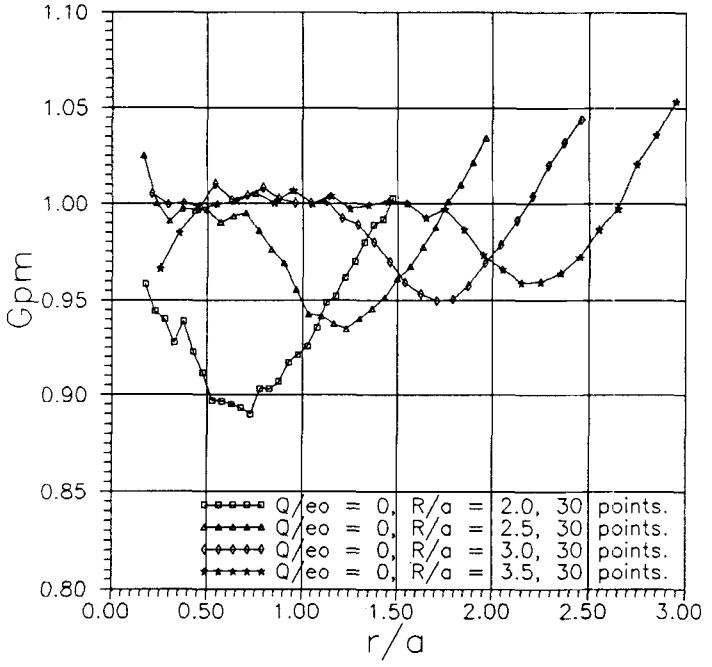

Figure 8 G_{pm} for chargeless pores with $R/a = 2.0, 2.5, 3.0$ and 3.5. There can be no electro desorption here, so the increasing depression of the curves with decreasing radii must be caused by the ionic cloud asymmetry repulsion from the wall. Compared to Figure 3 the depressions are smaller, since the Debye length is shorter. $B = 1.681$, $\rho^* = 0.09248$.

based on compressibility, which should be slightly better than the Percus-Yevick compressibility expression [12]:

$$\mu(\text{ex, CS, com.})/kT = [3\eta^3 - 9\eta^2 + 8\eta]/[1-\eta]^3 \tag{6}$$

$$\mu(\text{ex, PY, com.})/kT = 3[\eta/(1-\eta)]^3 + 7.5[\eta/(1-\eta)]^2 + 7[\eta/(1-\eta)] - \ln(1-\eta) \tag{7}$$

$$\eta \equiv \pi\rho^*/6 \tag{8}$$

The CS-value (0.42548) and the PY-value (0.42566) are both inside the uncertainty range of the canonical ensemble test particle values simulated for a number of "ions" $N = 32, 64$ and 120 with $B = 0$, see footnote *b* below Table 1. We adopt the following value:

$$\mu(\text{ex}, B = 0, \rho^* = 0.09248)/kT = 0.4255 \pm 0.0010 \tag{9}$$

That the input for the GCEMC simulation is correct, is demonstrated for the larger pores in Figure 13. There is clearly a large central part of the pore, where G_{pm} fluctuates around unity.

Apart from that, Figure 13 exhibits the "hard wall/hard sphere attraction" in pure form. The relative concentrations at the wall are much higher than in the corresponding systems with $B = 1.681$. There is a very slight depression below unity with a minimum around 1 a-unit from wall contact, but this depression has nothing to do with the

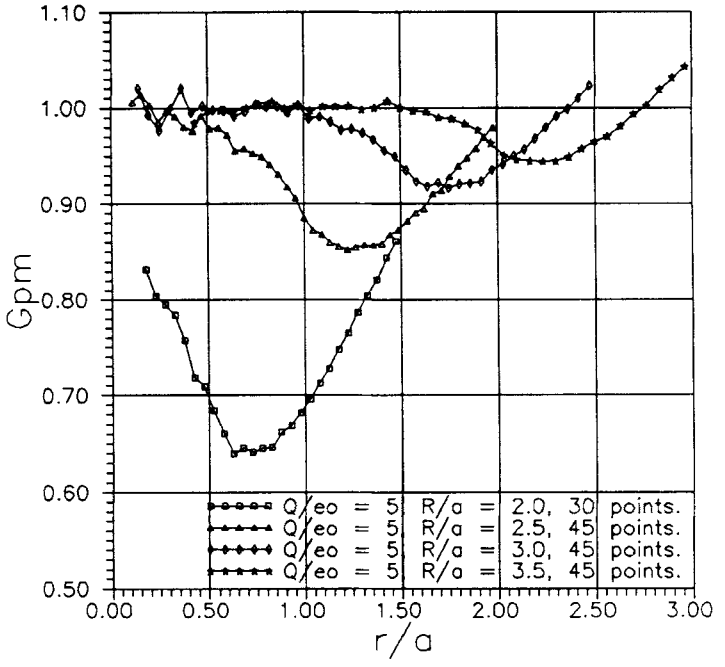

Figure 9 G_{pm} for pores with a surface charge = 5 units and $R/a = 2.0, 2.5, 3.0$ and 3.5. Compared to Figure 4 it is seen, that corresponding curves ($R/a = 2.0$ and 3.0) are almost unaffected by the concentration, except near the wall where the upward bents are more pronounced for the high concentration. $B = 1.681$, $\rho^* = 0.09248$.

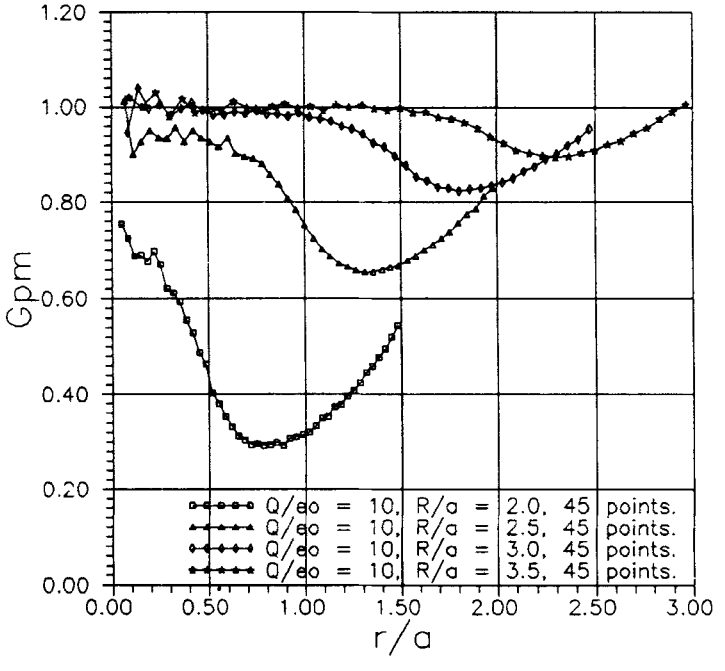

Figure 10 Same as Figure 9, but with $Q/e_0 = 10$. Compared to Figure 9, a very pronounced electrodesorption is found for the smallest pores. $B = 1.681$, $\rho^* = 0.09248$.

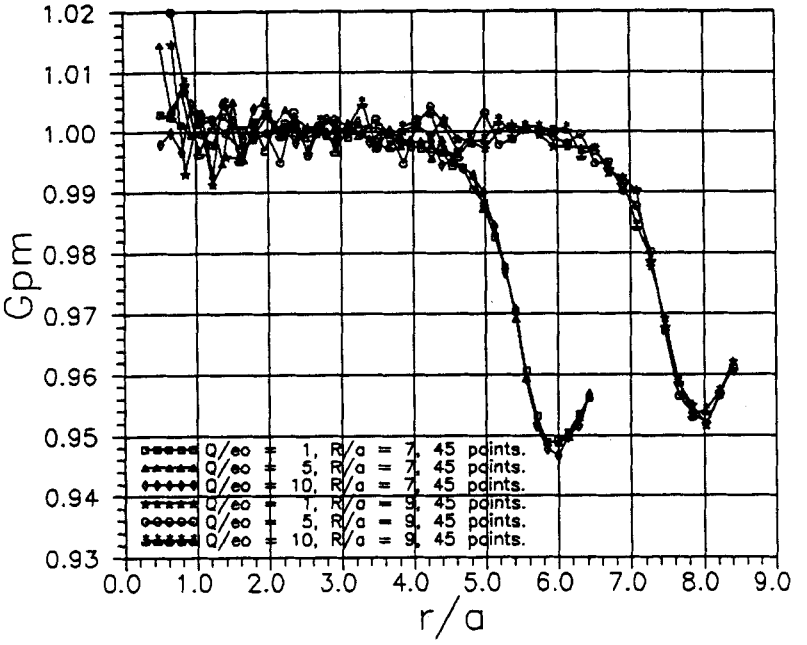

Figure 11 G_{pm} for large pores with $R/a = 7$ and 9 at the lower concentration and surface charges 1, 5 and 10 units. No electro-desorption is visible. Bulk properties prevail except for a narrow surface region. $B = 1.681$, $\rho^* = 0.0393$.

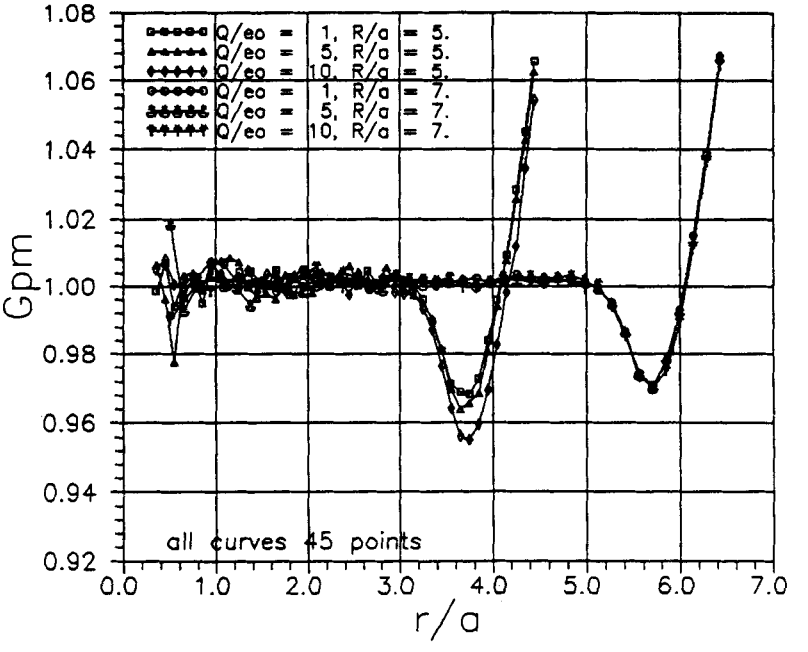

Figure 12 G_{pm} for pores with $R/a = 5$ and 7 at the higher concentration and surface charges 1, 5 and 10 units. No electro-desorption is visible for the larger pore. Some electro-desorption is seen in the surface region of the smaller pore, whereas the central "bulk region" is not affected. $B = 1.681$, $\rho^* = 0.09248$.

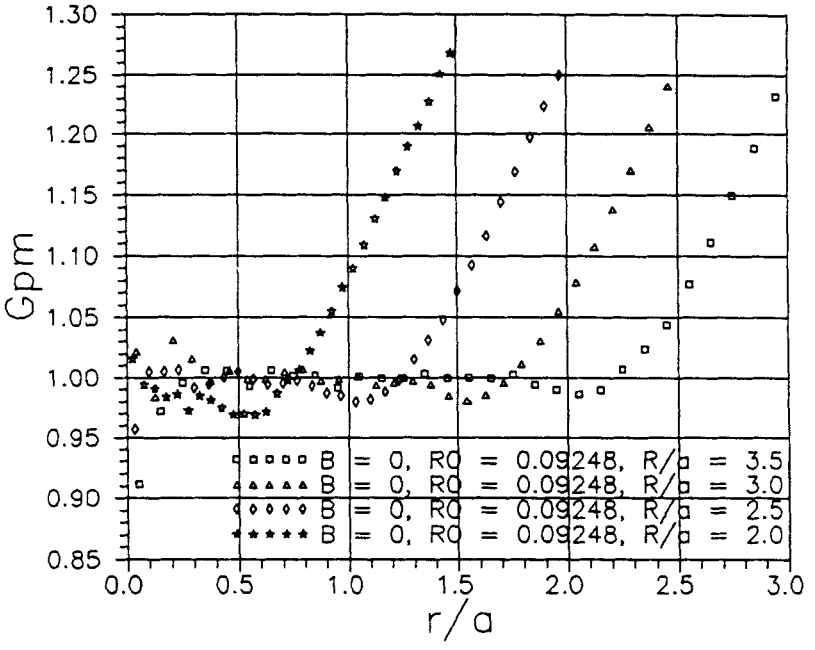

Figure 13 G_{pm} for pores with $R/a = 2.0, 2.5, 3.0$ and 3.5 and chargeless particles at the higher concentration exhibiting the "hard sphere/hard wall attraction" in pure form. See also Figure 32 and the discussion. $B = 0$ and $\rho^* = 0.09248$.

dramatic depressions due to the asymmetric ionic cloud effects in ionic systems (Figures 8–10). Especially it is seen, that even for the smallest pores, the value of G_{pm} in the center is unity (or very close to) for chargeless particles in contrast to the situation for charged particles (even when $Q/e_0 = 0$, see Figure 8).

CALCULATION OF THE ELECTRIC POTENTIAL DISTRIBUTION FROM ΔG

From the dimensionless and scaled electric charge density ΔG it is possible to calculate the electric potential profile in the pore. The Poisson equation in the case of a spherically symmetric charge distribution may be "solved" in terms of integrals over the first and the second moments of the charge density, see reference 1, Equations (23–27) and Equations (73–76). (See also reference 11, appendix, for a similar calculation of the electric potential distribution *around* ions from MC data). The result is

$$\Phi(t) = e_0\Psi(t)/k_BT = B(Q/e_0)(a/R) + \Delta + 0.5(\kappa a)^2[I_1(t) + I_2(t)] \tag{10}$$

$$I_1(t) = (1/t)\int_0^t s^2\Delta G(s)\,ds; \quad I_2(t) = \int_t^\infty s\Delta G(s)\,ds \tag{11}$$

Φ is the dimensionless total potential which consists of a (constant) contribution from the wall charge, any possible additional applied potential (Δ) and the contribution from the diffuse electric double layer. The latter is expressed through the two integrals in

Equation (11). We have $\tau = (R/a) - (1/2)$. (Note , there is a misprint in reference 1, Equation (75). The lower limit in the last integral is t, *not* 1). Thus, from GCEMC data for $\Delta G(t)$, it is possible to calculate the potential distribution in the spherical electric double layer by numeric integration. Such an integration has a considerable smoothing effect on the ΔG-data, which may be somewhat "noisy"-especially in the middle of the pores, where the shell volume is small.

In practice, we have fitted a least square polynomial at lowest possible degree with zero slope in $t = 0$ (for symmetry reasons) which fits smoothly the data and does not introduce false oscillations to the $\Delta G(t)$ data, and then we performed the integrations analytically. For some large pores, there is a wide central region, where bulk properties prevail, and we have "noisy" fluctuations around $\Delta G = 0$. In such cases it is better to put $\Delta G = 0$ in this region in the integrals (11) and use a polynomial fit for the "surface region". The results will be shown in a short while, but first we shall consider a possibility to express the charge density as well as the electric potential in terms of eigenfunctions of the Laplace operator in the interior of a sphere.

In dimensionless variables, the Poisson equation may be written (for a 1:1 electrolyte):

$$\nabla^2 \Phi = d^2\Phi/dt^2 + (2/t)\, d\Phi/dt = -0.5\,(\kappa a)^2\, \Delta G \tag{12}$$

Now assume, that the potential may be expressed as a sum over eigenfunctions to the Laplacian (with no angular dependence and with a constant added) inside a sphere:

$$\Phi = A_o + \textstyle\sum_k A_k \sin h(\lambda_k a t)/(\lambda_k a t) \tag{13}$$

or-using the limiting behaviour of $\sin h(x)/x$ for $x \to 0$—we have:

$$\Phi = \Phi(o) + \textstyle\sum_k A_k \{[\sin h(\lambda_k a t)/(\lambda_k a t)] - 1\} \tag{14}$$

$\Phi(o)$ is the dimensionless potential in the middle of the pore. We use the mathematical property

$$\nabla^2 \{\sin h(\lambda_k a t)/(\lambda_k a t)\} = (\lambda_k a)^2 \{\sin h(\lambda_k a t)/(\lambda_k a t)\} \tag{15}$$

and obtain from (12–13):

$$\nabla^2 \Phi = \textstyle\sum_k A_k (\lambda_k a)[\sin h(\lambda_k a t)/t] = -0.5\,(\kappa a)^2\, \Delta G$$

Thus, the dimensionless charge density is given as:

$$\Delta G = -(2[\kappa a]^{-2}) \textstyle\sum_k (\lambda_k a)\, A_k \sin h(\lambda_k a t)/t \tag{16}$$

In some cases, oscillations appear in the charge density and in the potential. Then it may be necessary to use couples of complex conjugate eigenvalues (to obtain real potentials and charge densities):

$$\lambda_{k,\pm} = \alpha_k \pm i\beta_k \tag{17}$$

with a common, real constant A_k. Equation (16) may then be written in the following form:

$$\Delta G = +(4t^{-1}[\kappa a]^{-2}) \textstyle\sum_k A_k \{\beta_k a \cos h(\alpha_k a t) \sin(\beta_k a t) - \alpha_k a \sin h(\alpha_k a t) \cos(\beta_k a t)\} \tag{18}$$

The values of ΔG obtained in this manner should be (statistically) equivalent to the values obtained directly from the GCEMC simulations, but they are smoothed values.

We shall never use more than two eigenfunctions (possibly complex conjugate couples). Since we know the potential at wall contact, $t = \tau = (R/a) - 0.5$, the constant A_1 may be calculated from:

$$A_1 = \{\Phi(\tau) - \Phi(o) - A_2 f_2(\tau)\}/f_1(\tau) \tag{19}$$

$$f_1(\tau) = [\sinh(\lambda_{1,+}\, a\tau)/(\lambda_{1,+}\, a\tau) + \sinh(\lambda_{1,-}\, a\tau)/(\lambda_{1,-}\, a\tau) - 2] \tag{20}$$

$$f_2(\tau) = [\sinh(\lambda_{2,+}\, a\tau)/(\lambda_{2,+}\, a\tau) + \sinh(\lambda_{2,-}\, a\tau)/(\lambda_{2,-}\, a\tau) - 2] \tag{21}$$

The functions $f_1(\tau)$ and $f_2(\tau)$ are both real valued, so that A_1 is real. If the potential may be adequately described by only one eigenfunction or by a complex conjugate couple, A_2 is put equal to zero in (19).

In pores with dilute solutions (but not necessarily small dimensionless potentials) it is possible to calculate λ from Φ_0 and a "generalized Debye-Hückel equation", see reference 1, Equation (63) and reference 1, Figure 19.

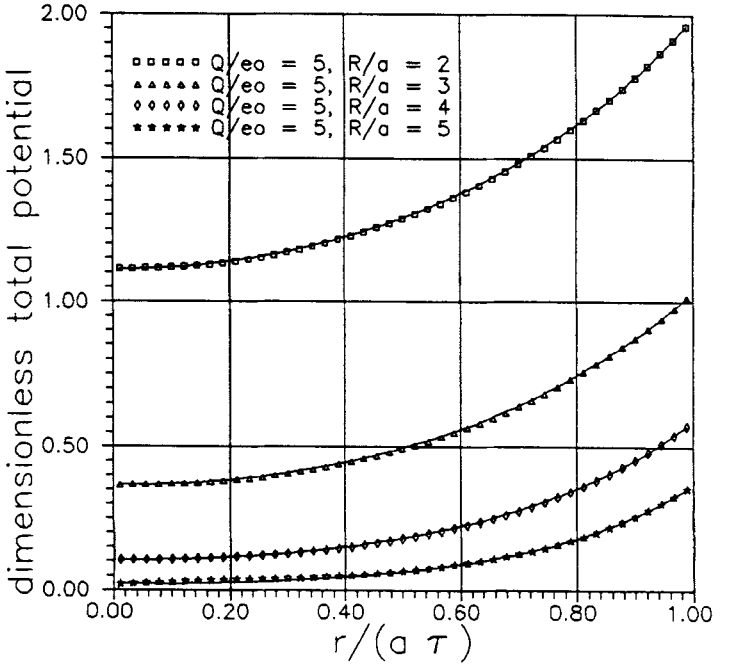

Figure 14 The dimensionless total potential as a function of t/τ for pores with a surface charge of 5 unit charges and $R/a = 2$, 3, 4 and 5 at the lower concentration ($\tau = [R/a] - 0.5$). The full curves are calculated from the eigenfunction fits (see Table 3). All potential profiles in this and in the following figures have been based on simulated ΔG values contracted in 30 shells and fitted with least square polynomials with zero slope for $r/a = 0$. This is true even if more than 30 calculated points are shown. $B = 1.681$ and $\rho^* = 0.0393$.

ELECTRIC POTENTIAL AND CHARGE DENSITY PROFILES

Figure 14 shows the dimensionless total potential in pores with $R/a = 2, 3, 4$ and 5 for a wall charge of five units and a concentration $\rho^* = 0.0393$. The displacements mostly reflect the variation in the part of the potential induced by the wall charge in an ion free system. In the smaller pores, the pore radius is not large enough for an efficient screening of the wall charge in the middle of the pore, so the central potential $\Phi(o)$ is considerably above zero. In the largest pore, the central potential is close to zero. The screening is efficient, since the pore radius is ca. 4.5 Debye lengths. A similar behaviour is seen for a wall charge of 10 units (Figure 15), but the potentials at contact $\Phi(\tau)$ are considerably higher. In Figures 14 and 15, the points are calculated points from fitting the integrands (with the "experimental" ΔG's) in Equation (11) to least square polynomials with zero slope in the center and performing the integrations analytically. The curves drawn in Figures 14 and 15 are eigenfunction fits (described in the previous section). All the data for these fits (also for the following figures) have been collected in Table 3.

Figure 16 shows the "experimental" ΔG's vs. $t = r/a$ in the case $B = 1.681$, $\rho^* = 0.0393$, $Q/e_0 = 10$. The curves correspond to the eigenfunction fits in Figure 15 as calculated from Equation (18). It should be mentioned, that it is often possible to fit the potential curves equally well with several different choices of a single eigenfunction, but if the corresponding ΔG-curves should also be well fitted, the choice is much more restricted.

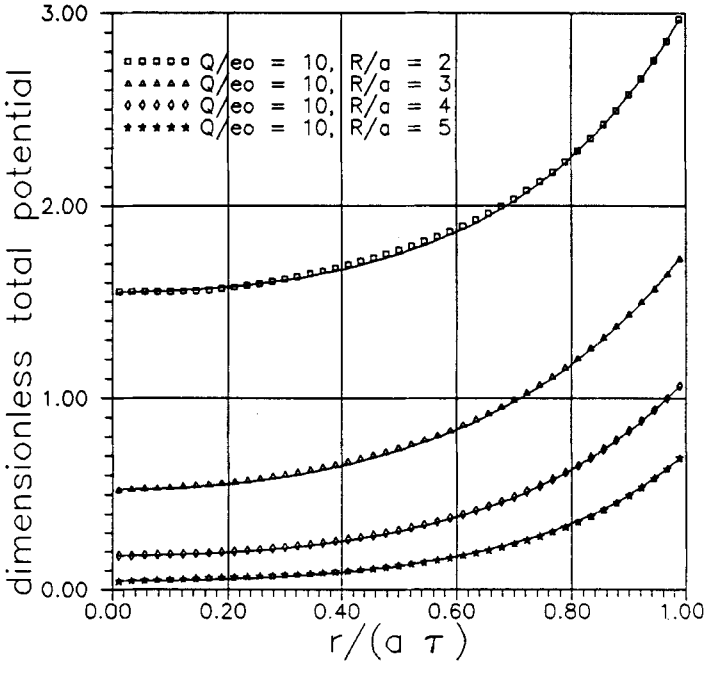

Figure 15 The same as Figure 14, but with a surface charge equal to 10 unit charges.

Table 3 Eigenfunction parameters for potential profiles and for ΔG; $B = 1.681$.

κa	Q/e_0	R/a	$\phi(0)$	$\phi(\tau)$	$\alpha_1 a/\kappa a$	$\beta_2 a/\kappa a$	A_2	*further comments*
0.9111	1	7.0	(0)	3.61e − 2				
0.9111	1	9.0	(0)	(2.1201e − 2)				
0.9111	5	2.0	1.1114e + 0	1.9838e + 0	1.7	0.0	0.0	$\Phi(t)$ and $\Delta G(t)$ well fitted
0.9111	5	3.0	3.6608e − 1	1.0322e − 1	1.0	0.25	1.5	$\Phi(t)$ well fitted, $\Delta G(t)$ not perfect
0.9111	5	4.0	1.0377e − 1	5.8762e − 1	1.0	0.25	0.3	$\Phi(t)$ and $\Delta G(t)$ well fitted
0.9111	5	5.0	2.0925e − 2	3.6962e − 1	1.0	0.20	0.19	$\Phi(t)$ well fitted, $\Delta G(t)$ not perfect
0.9111	5	7.0	(0)	1.82e − 1				
0.9111	5	9.0	(0)	1.06e − 1				
0.9111	10	2.0	1.5485e + 0	3.0231e + 0	3.0	0.0	0.0	$\Phi(t)$ well fitted, $\Delta G(t)$ not perfect
0.9111	10	3.0	5.2867e − 1	1.7646e + 0	1.5	0.0	0.0	$\Phi(t)$ and $\Delta G(t)$ very well fitted
0.9111	10	4.0	1.7669e − 1	1.0963e + 0	1.0	0.25	1.6	$\Phi(t)$ and $\Delta G(t)$ very well fitted
0.9111	10	5.0	4.3514e − 2	7.1764e − 1	1.0	0.18	0.59	$\Phi(t)$ and $\Delta G(t)$ very well fitted
0.9111	10	7.0	(0)	3.60e − 1				
0.9111	10	9.0	(0)	2.11e − 1				
1.3977	1	5.0	(0)	3.93e − 2				
1.3977	1	7.0	(0)	2.05e − 2				
1.3977	5	2.0	3.1742e − 1	1.3231e + 0	1.0	1.0	0.39	$\Phi(t)$ and $\Delta G(t)$ very well fitted
1.3977	5	2.5	6.1650e − 2	8.5650e − 1	1.0	1.05	0.103	$\Phi(t)$ and $\Delta G(t)$ very well fitted
1.3977	5	3.0	1.6056e − 2	5.8680e − 1	1.0	0.8	0.14	$\Phi(t)$ and $\Delta G(t)$ well fitted
1.3977	5	3.5	7.2137e − 3	4.2455e − 1	1.0	0.8	0.08	$\Phi(t)$ and $\Delta G(t)$ very well fitted
1.3977	5	5.0	(0)	1.96e − 1				
1.3977	5	7.0	(0)	1.01e − 1				
1.3977	10	2.0	6.9743e − 1	2.2397e + 0	2.6	0.3	− 3.3	$\Phi(t)$ well fitted, $\Delta G(t)$ not perfect
1.3977	10	2.5	1.3560e − 1	1.5268e + 0	1.55	0.0	0.0	$\Phi(t)$ and $\Delta G(t)$ very well fitted
1.3977	10	3.0	1.8800e − 2	1.0971e + 0	1.0	0.3	2.2	$\Phi(t)$ and $\Delta G(t)$ very well fitted
1.3977	10	3.5	1.4432e − 2	8.1418e − 1	1.0	0.3	1.2	$\Phi(t)$ and $\Delta G(t)$ very well fitted
1.3977	10	5.0	(0)	3.90e − 1				
1.3977	10	7.0	(0)	2.01e − 1				

$\beta_1 = \alpha_2 = 0$ in all cases

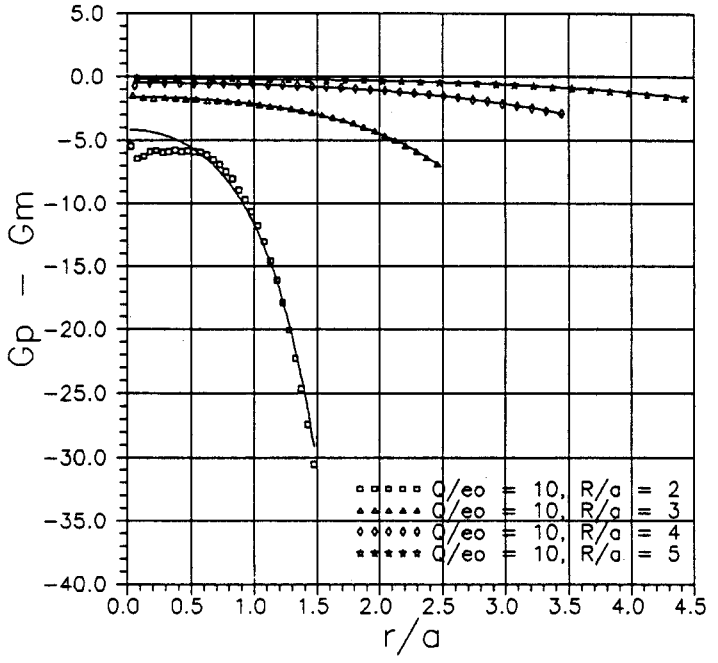

Figure 16 The simulated $\Delta G(t)$ values on which Figure 15 was based. The full curves are calculated from the eigenfunction fits, see Table 3 and Equation (18).

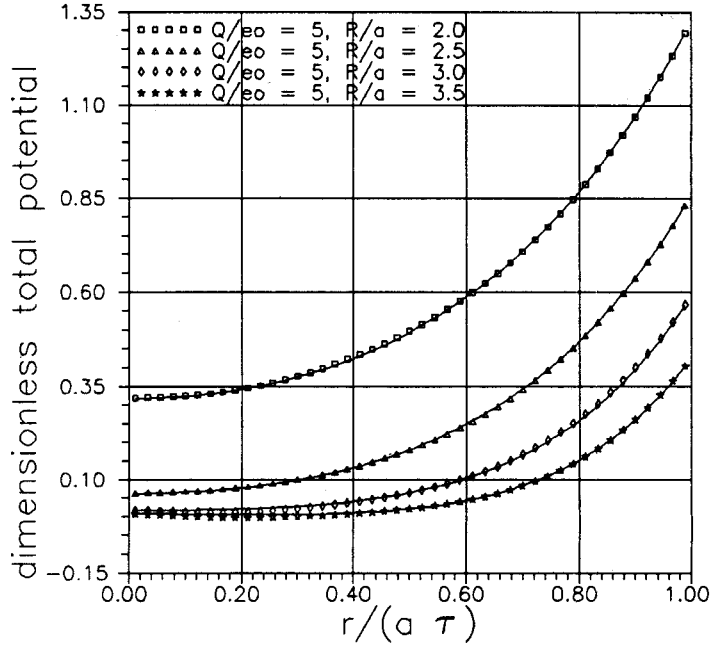

Figure 17 The dimensionless total potential profiles for a surface charge of 5 units and $R/a = 2.0$, 2.5, 3.0 and 3.5 at the higher concentration. Full curves are eigenfunction fits. $B = 1.681$ and $\rho^* = 0.09248$.

Figure 17 shows the potential profiles in the case $B = 1.681$, $\rho^* = 0.09248$, $Q/e_0 = 5$ and $R/a = 2, 2.5, 3, 3.5$. Again, the contact potential as well as the center potential is depressed for increasing radius, and for the larger pores the center potential is close to zero. For the largest pores, there is a slight tendency for the potential to decrease to very small negative values before the rise towards the contact potential. Figure 18 is similar, but for $Q/e_0 = 10$. The contact potentials are here larger for the same pore sizes and the potential minimum for the largest pore is quite insignificant. Comparing Figure 17 to Figure 14 and Figure 18 to Figure 15, we observe that the contact potentials decrease with increasing concentration for the same pore size and wall charge as the case is for a plane, diffuse double layer. The "experimental"ΔG-values corresponding to the potentials in Figure 18 are shown in Figure 19 together with the curves calculated from the eigenfunction fits to the potential profiles.

For the larger pores and/or higher concentrations, there are problems with obtaining ΔG-data in the central part of the pore, which are precise enough for a reliable determination of the potential profile. Figure 20a shows the ΔG-data for pores with $\rho^* = 0.0393$, $Q/e_0 = 1$ and $R/a = 7$ and 9. A total number of configurations of 480 millions and 120 millions of configurations have been performed. Even with this large number of configurations, the "noise" in the middle of the pore is considerable. However, after the first few extreme deviations, the values seem to fluctuate around zero. Figure 20b shows a reasonable replacement of the first ΔG-values with zeros.

Figure 21 shows tentative calculations of the potential profiles for the two pores. The open symbols have been calculated fitting the unadjusted $t \cdot \Delta G(t)$ and $t^2 \cdot \Delta G(t)$ data

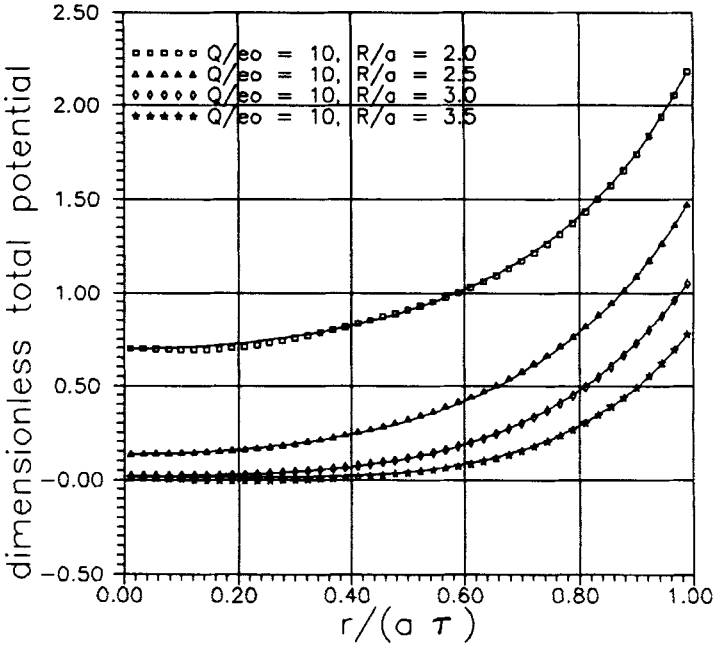

Figure 18 The same as Figure 17, but with 10 unit charges.

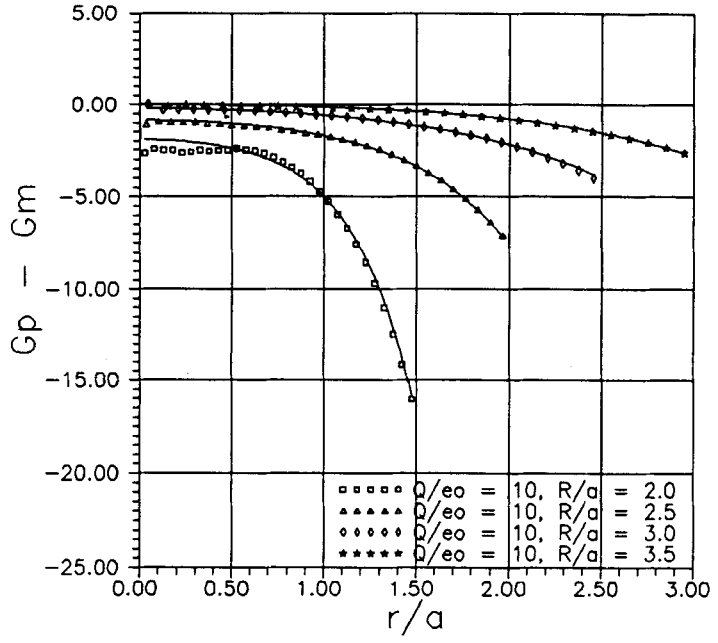

Figure 19 The $\Delta G(t)$ values on which Figure 18 was based. Full curves are eigenfunction fits.

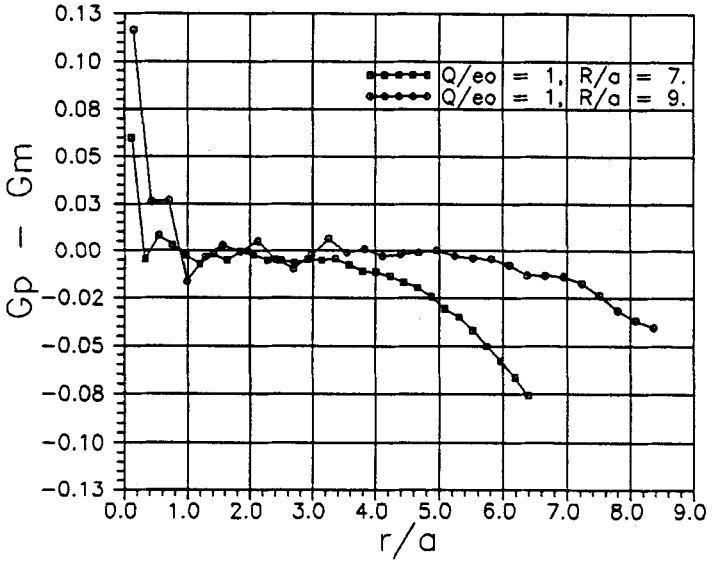

Figure 20a The simulated $\Delta G(t)$ values for pores with a surface charge of one unit and $R/a = 7$ and 9 at the lower concentration. In the middle of the pore the fluctuations are great, and the values also seem to be systematically too high. Thus, complete statistical equilibrium may not have been reached here in spite of the high number of configurations (480 millions for $R/a = 7$ and 120 millions for $R/a = 9$). The curve with the higher number of configurations seems a little better, however. $B = 1.681$ and $\rho^* = 0.0393$.

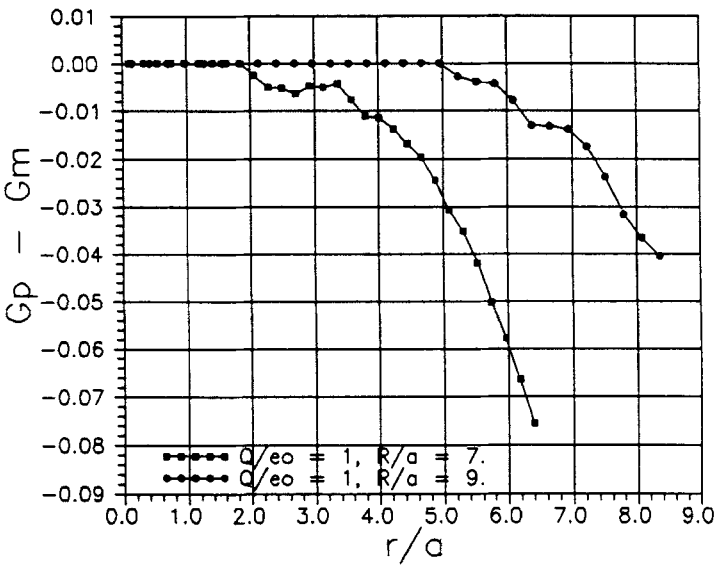

Figure 20b The same as Figure 20a, but with the most central values of ΔG replaced by zeros. Zeros are inserted at all values, which seem to fluctuate around zero in Figure 20a. When the first systematic deviation from zero is visible in Figure 20a, the simulated ΔG's are used.

(both contracted to 30 shells) to least square polynomials of degree six with zero slope in the center. These polynomials are then used for analytical integration in Equation (11). The corresponding black symbols are calculated by the adjusted data of Figure 20b. Least square polynomials of degree 6 with zero initial slope are found again for the adjusted $t \cdot \Delta G(t)$ and $t^2 \cdot \Delta G(t)$ data, but the part of the integrals where $\Delta G = 0$ are put to zero. The difference between the two curves is a measure of the uncertainty in the potential determination. This uncertainty is very large in the central part of the pore, but for physical reasons, we assume the potential to be zero (or close to) in the central part, since the wall charge is effectively shielded. The pore with $R/a = 7$ seems to have a well defined potential near the wall, however, whereas even the contact potential $\Phi(\tau)$ is quite uncertain for the pore with $R/a = 9$.

Figures 22 and 23 show the potential distributions and the ΔG values for the same cases, but with $Q/e_0 = 5$. Here, the determination of the potential profiles seems to be precise, except in the most central part. The same can be said for $Q/e_0 = 10$ (Figures 24 and 25).

The same pattern repeats itself for the high concentration, where the same three charges have been investigated for pores with $R/a = 5$ and 7 (Figures 26–31). In general it is seen, that there is no reason to believe, that the charge densities and the potentials

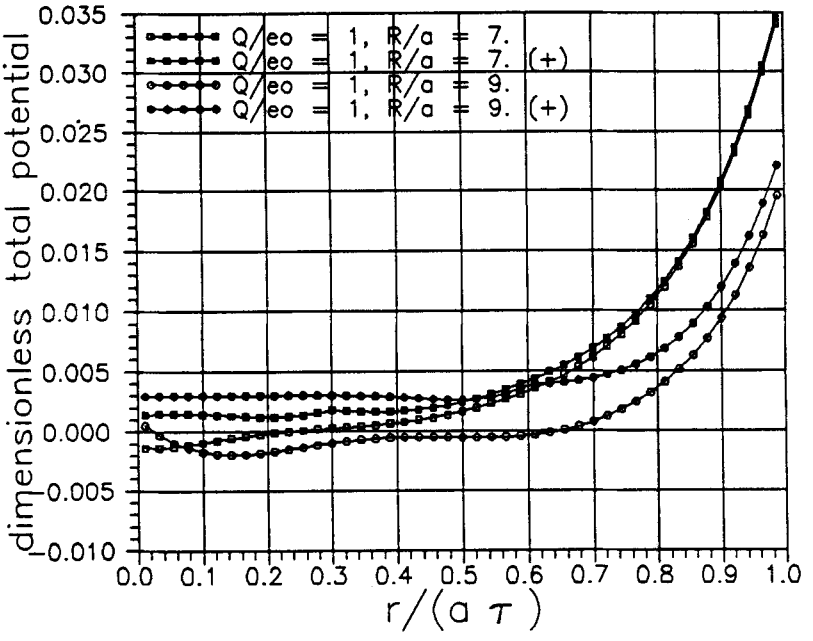

Figure 21 Tentative dimensionless total potential profiles calculated from the data of Figures 20a and 20b. White symbols correspond to the use of polynomial fits to the uncorrected ΔG data of Figure 20a. The black symbols (with a + mark) correspond to the use of the corrected data of Figure 20b. The larger pore ($R/a = 9$) has an uncertain potential profile in the whole range. The smaller ($R/a = 7$) seems quite well determined near the wall, but not in the middle. Most probably, the potentials are zero (or close to) in the central part of the pores. $B = 1.681$ and $\rho^* = 0.0393$. $Q/e_0 = 1$.

are not zero in a central region of these large pores. Furthermore, the contact potential $\Phi(\tau)$ decreases with increasing concentration or pore radius.

DISCUSSION

We have fitted the potential profiles and the charge density profiles to eigenfunctions of the Laplacian for all pores except the largest, where there is considerable uncertainty in the central part of the potential. Either one eigenfunction with a real eigenvalue or two sets of eigenfunctions with complex conjugate eigenvalues have been used. In the latter case, it is always sufficient with one purely real and one purely imaginary eigenvalue, and in many cases, the real eigenvalue may be chosen as the inverse Debye length, see Table 3. The fits are good or even excellent, although in some few cases the $\Delta G(t)$ data were not perfectly fitted in the middle of the pore (and better fits were apparently not possible with only to sets of eigenfunctions).

According to Table 3, the contact potential $\Phi(\tau)$ and the center potential $\Phi(0)$ decrease with increasing concentration and with increasing pore radius for the same

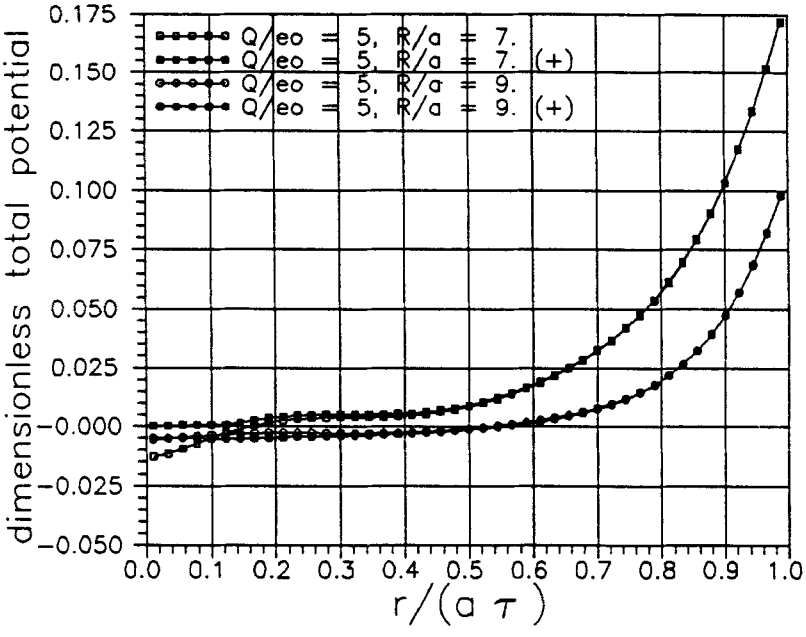

Figure 22 The same as Figure 21, but with $Q/e_0 = 5$. The black and white symbols coincide except in the most central part. $B = 1.681$ and $\rho^* = 0.0393$.

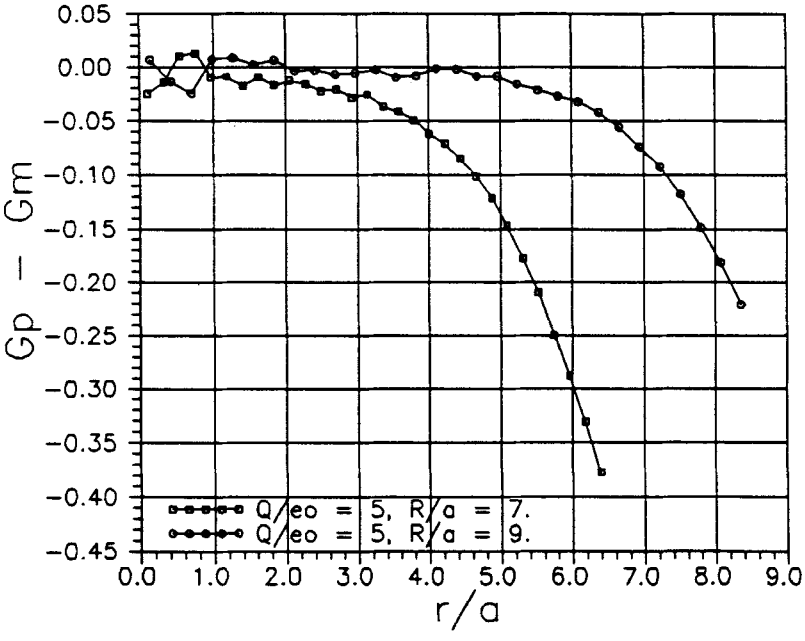

Figure 23 The $\Delta G(t)$ values on which Figure 22 is based. The values in the middle seems much better in statistical equilibrium than the ones for $Q/e_0 = 1$ (Figure 20a). For $R/a = 7$, ΔG up to $t = 0.7$ have been put equal to zero in the calculation of the black squares in Figure 22. For $R/a = 9$, ΔG up to $t = 1.9$ have been put equal to zero in the calculation of the black circles in Figure 22.

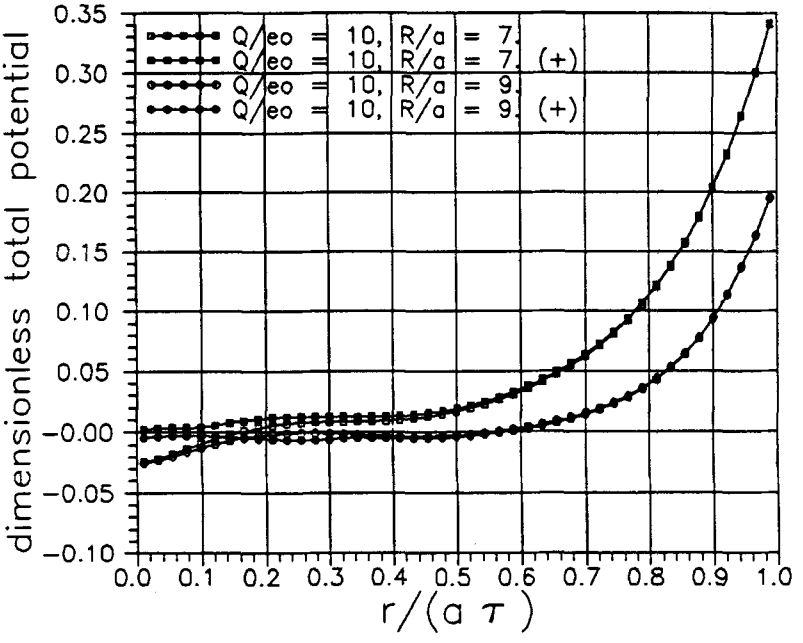

Figure 24 The same as Figure 22, but with $Q/e_0 = 10$. The black and white symbols coincide except in the most central part. $B = 1.681$ and $\rho^* = 0.0393$.

surface charge. Increasing the surface charge, the two potentials increase. In the larger pores, the surface charge is effectively Debye shielded in the middle, so that the center potential is equal to zero or close to. For the largest pores this may be difficult to prove definitively by simulation because of the "noise" in the central $\Delta G(t)$ data.

The determination of the potential profile in the central part of the large pores seems to be an almost unsurmountable problem at the present concentration of electrolytes. Most probably, the potential oscillations reported for the largest pores in an earlier paper [1] for these systems for $Q/e_0 = 1$ are fake phenomena. In this paper never more than 50 millions of configurations were applied. Furthermore, cubic splines were used to fit the data for $t \cdot \Delta G(t)$ and $t^2 \cdot \Delta G(t)$ in the two integrations. This is a local method, where pieces of cubic polynomials are spliced together to have the same first and second derivatives in the splicing points. The fluctuations in the data are followed exactly. Although the datasets $t \cdot \Delta G(t)$ and $t^2 \cdot \Delta G(t)$ have much less relative noise in the center, than the set of $\Delta G(t)$, and although the integrations tend to smoothe out fluctuations, the reason for the oscillations seems to be the erratic and possibly also systematically deviating ΔG values in the central part. Even for the high number of configurations used here, there seems to be a tendency for the ΔG values to be too high in the middle for the larger pores.

There is no physical reason that ΔG should have a "positive hump" in the middle of a pore for a large pore, when it has been shown for a succession of smaller pores, that the

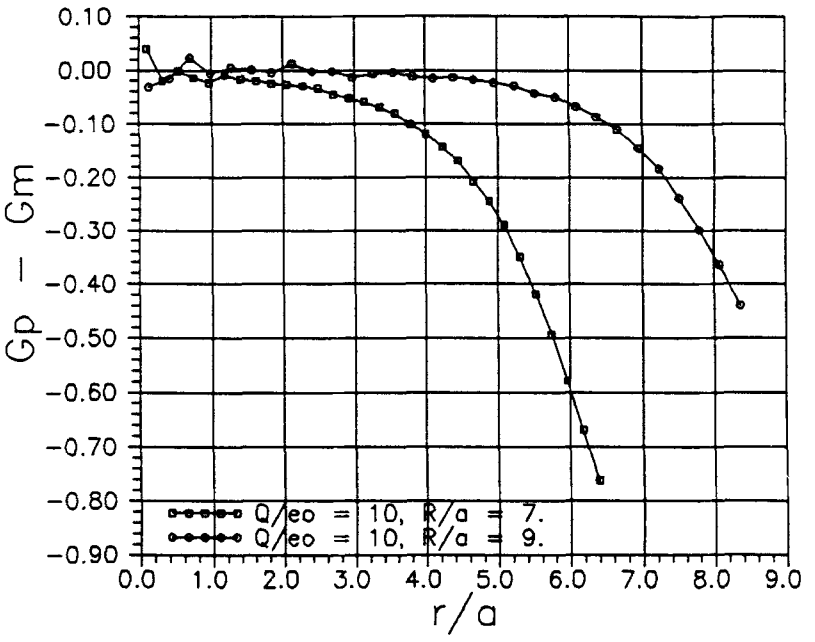

Figure 25 The $\Delta G(t)$ values on which Figure 24 is based. The values in the middle seems much better in statistical equilibrium than the ones for $Q/e_0 = 1$ (Figure 20a). For $R/a = 7$, ΔG up to $t = 0.6$ have been put equal to zero in the calculation of the black squares in Figure 24. For $R/a = 9$, ΔG up to $t = 2.7$ have been put equal to zero in the calculation of the black circles in Figure 24.

potential in the central part comes closer and closer to zero with increasing radii as expected (Debye shielding). We have tried the cubic spline method on the present data—with a much higher number of configurations—and quite similar oscillations to the oscillations shown in reference [1] Figures 22–23 and 27–28 may be produced. The underlying problem is, that the electrostatic fields are weak for $Q/e_0 = 1$ and large pores, but the value of the potential in the central part is a sensitive functional of the charge distribution all over the pores. The method used here with global least square polynomials with zero slope in the middle and with sensitivity tests comparing potentials from uncorrected data with potentials calculated from data with a reasonable number of central ΔG values forced to be zero seems to be a more healthy procedure.

The $G_{pm}(t)$ data are dominated by three main features: The "mean ions" seem to avoid the wall region, since they cannot form symmetric ionic clouds in that region. Contrary to this, the mean ions seem to be squeezed up against the pore wall by the somewhat unidirected hard sphere collisions on an ion close to the wall. The latter effect is more pronounced for higher than for lower concentrations. Finally, most pronounced for small pores, there is an electro-desorption effect. The G_{pm} curves are depressed by increasing the wall charge. The electro-desorption is more marked for the higher concentrations. For large pores, however, there is no dependence of G_{pm} on the

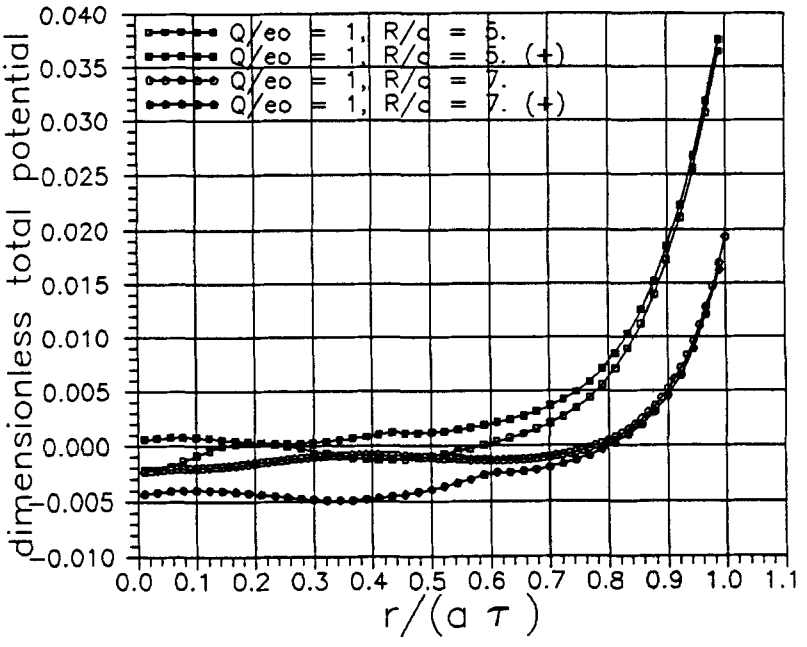

Figure 26 Tentative dimensionless total potential profiles calculated from the data of Figure 27. High concentration and a surface charge of one unit. $R/a = 5$ and 7. White symbols correspond to the use of polynomial fits to the uncorrected ΔG data. The black symbols (with a + mark) correspond to the use of data with the central ΔG's put equal to zero. Both pores have no well determined potential profiles except close to the wall. Most probably, the potentials are zero (or close to) in the central part of the pores. $B = 1.681$ and $\rho^* = 0.09248$. $Q/e_0 = 1$.

wall charge (between 1 and 10 units), see Figure 11 (only $R/a = 7$) and Figure 12 (both curves).

Apart from the above mentioned phenomena, the G_{pm} data show the obvious fact, that in large pores there is a central part with "bulk properties" ($G_{pm} \approx 1$). It is perhaps somewhat surprising, that even quite small pores have a central "bulk region".

The simulations with $B = 0$ (Figure 13) may be used to subtract the pure hard sphere effects in order to demonstrate more clearly the "ion cloud asymmetry" effect. Assume, that the total dimensionless potential of mean forces for a "mean ion" defined by

$$W_{pm}(\text{tot}) \equiv -\ln G_{pm} \tag{22}$$

may be split into a hard sphere contribution

$$W_{HS} \equiv -\ln G_{pm}(B = 0) \tag{23}$$

and an "asymmetric ionic cloud" contribution W_{asym}.

$$W_{pm}(\text{tot}) = W_{HS} + W_{asym} \tag{24}$$

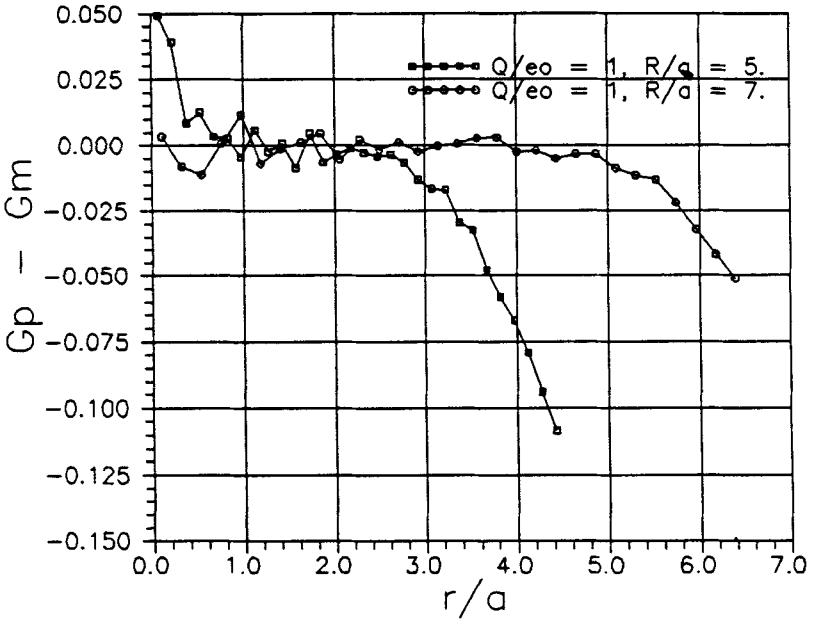

Figure 27 The $\Delta G(t)$ values on which Figure 26 is based. The values in the middle of the pore seem to be systematically too high for $R/a = 5$ (240 million configurations). For $R/a = 7$ (480 million configurations) ΔG seems to fluctuate around unity. For $R/a = 5$, ΔG up to $t = 1.9$ have been put equal to zero in the calculation of the black squares in Figure 26. For $R/a = 7$, ΔG up to $t = 3.8$ have been put equal to zero in the calculation of the black circles in Figure 26.

The last equation may be looked upon as just a definition of W_{asym}. Figure 32 shows $W_{asym}(t)$ for pores of four different sizes at the high concentration. The Debye length is ≈ 0.72 a-units for this system. For the largest pore ($R/a = 3.5$) it is seen, the W_{asym} has decreased to a fraction ≈ 0.29 of the values at wall contact at a distance one Debye length from the wall. If the decay was exponential in the wall distance measured in Debye lengths, the fraction should have been ≈ 0.37. For the pores with $R/a = 3.0$, 2.5 and 2.0, the corresponding fractions are 0.39, 0.39 and 0.50, respectively. Thus, the decrease is not really exponential. It seems more to be a linear decrease with an exponential tail. Furthermore, the "asymmetry potential" is stronger at contact for smaller pores than for larger. Also, the decay of the asymmetry potential is more marked for the smaller pores. This is naturally explained by the increased curvature of the wall in the small pores. In the pore with $R/a = 2$ an ion at wall contact is surrounded by a wall with high curvature destroying the formation of an ionic cloud not only in the radial direction, but also tangentially. For larger pores only half of the ionic cloud is directly destroyed.

It should be noticed, that these repulsive "asymmetry forces" near a wall are not at all accounted for in the classical theory of Onsager and Samaras [13]. In this theory the ions are predicted to withdraw from a plane surface, when a low dielectric permittivity

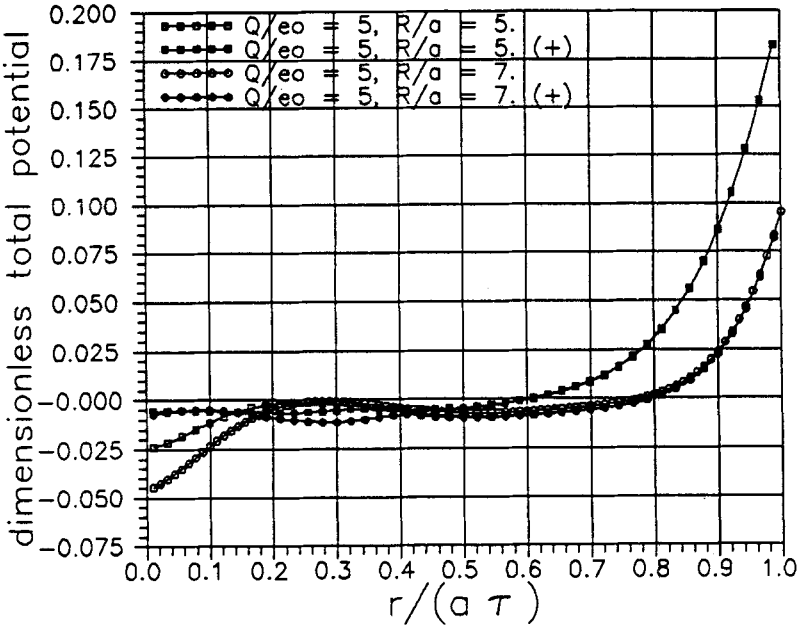

Figure 28 Same as Figure 26, but with a surface charge of 5 units. Black and white squares coincides above $t \approx 0.4$. The potential in the middle is probably zero (or close to). There is a weak indication of an intermediary region with negative potentials. $B = 1.681$ and $\rho^* = 0.09248$. $Q/e_0 = 5$.

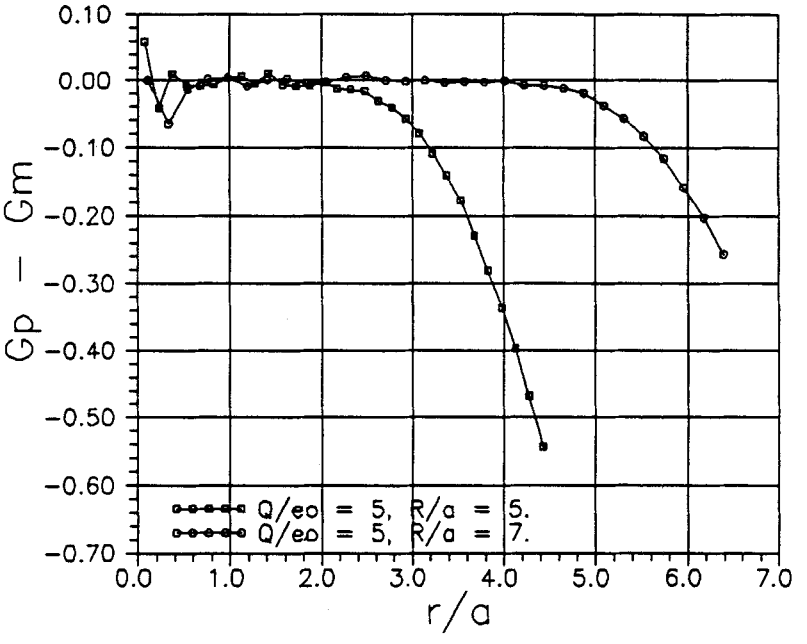

Figure 29 The $\Delta G(t)$ values on which Figure 28 is based. For $R/a = 5$, ΔG up to $t = 1.5$ have been put equal to zero in the calculation of the black squares in Figure 28. For $R/a = 7$, ΔG up to $t = 3.2$ have been put equal to zero in the calculation of the black circles in Figure 28.

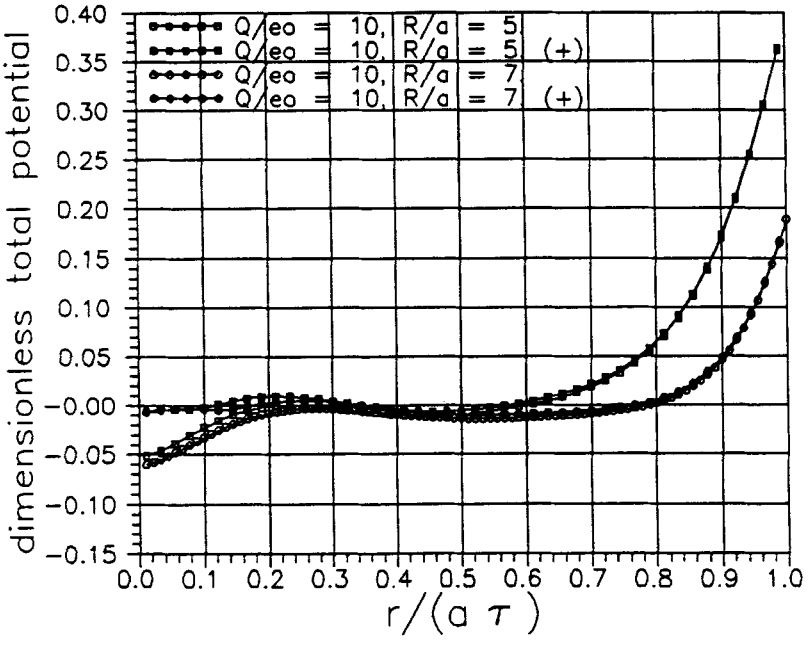

Figure 30 Same as Figure 26, but with a surface charge of 10 units. The potential in the middle is probably zero (or close to). There is some indication of an intermediary region with negative potentials. $B = 1.681$ and $\rho^* = 0.09248$. $Q/e_0 = 10$.

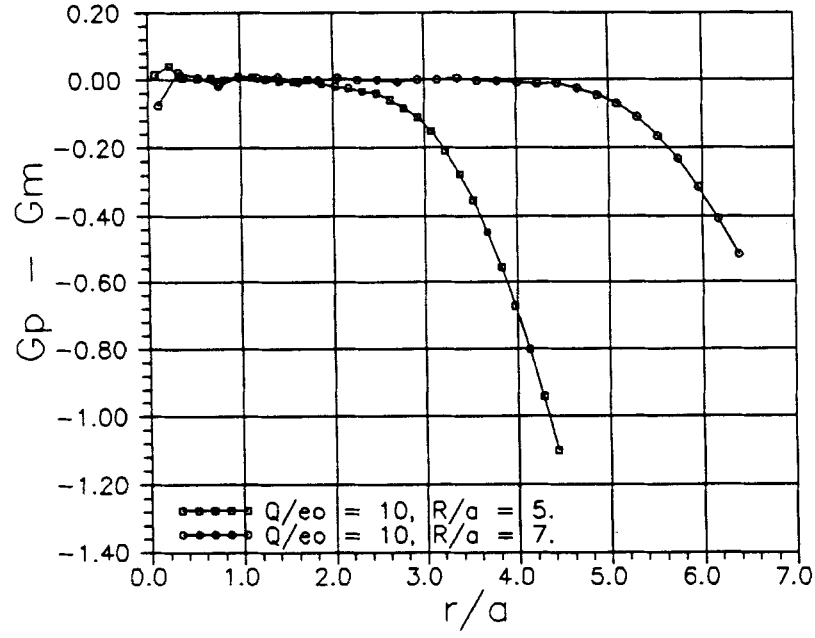

Figure 31 The $\Delta G(t)$ values on which Figure 30 is based. For $R/a = 5$, ΔG up to $t = 1.7$ have been put equal to zero in the calculation of the black squares in Figure 30. For $R/a = 7$, ΔG up to $t = 3.8$ have been put equal to zero in the calculation of the black circles in Figure 30.

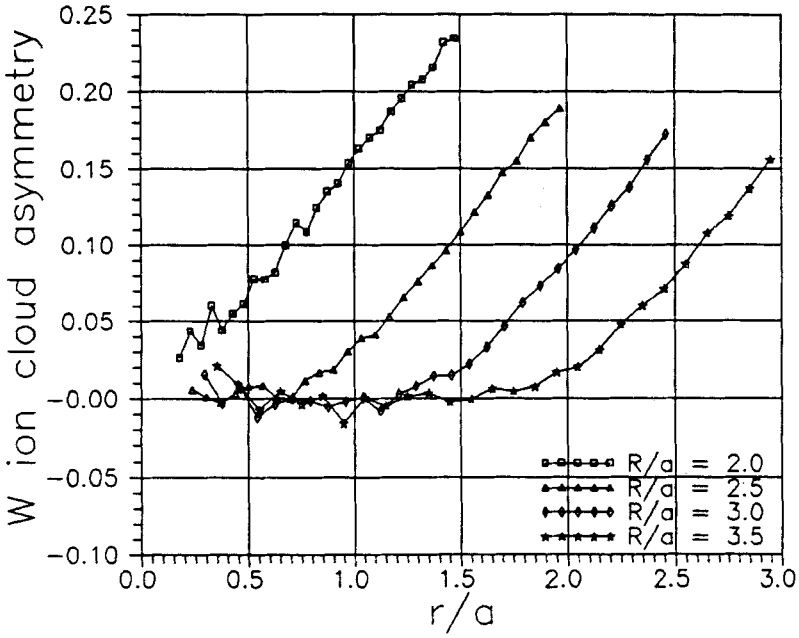

Figure 32 The dimensionless potential of mean forces corresponding to the repulsion of a "mean ion" from the wall because ions close to the wall cannot form a symmetric ionic cloud. W (asymm) = W_{tot} ($B = 1.681$, $Q/e_0 = 0$) − W_{HS}. The dimensionless potential of mean forces W_{HS} is calculated from the values of G_{pm} is Figure 13. High concentration and $R/a = 2.0$, 2.5, 3.0 and 3.5. The value of W (asymm) at contact increases with decreasing radius. The greater the wall curvature is, the greater part of the ionic cloud is directly destroyed for an ion in contact.

prevails at the other side of the surface (e.g. at a water-air interface). The reason is the (Debye shielded) interaction with the image charges of ions near the wall. However, the Onsager-Samaras effect disappears in the case, where the dielectric permittivity is identical on the two sides of the surface (no image charges). Figure 32 shows clearly, that there is an appreciable, effective repulsive potential also in the case of identical permittivities. Thus, the Onsager-Samaras theory cannot be considered to be complete even at the low electrolyte concentrations, for which it was intended. At low salt concentrations, the Debye length is very large, and the asymmetry zone very much extended. (In reference [1], Figure 5, the G_{pm} is shown for $B = 1.546$ and $\rho^* = 0.001$ for a pore with $R/a = 10$. The Debye length is here ≈ 7.2 a-units, and there is a considerable depression below unity of the G_{pm} curve in the whole pore except the most central part).

In a paper in preparation, we shall study occupation numbers, Donnan potentials and potential distributions in more dilute systems of 2:1 and 2:2 electrolytes, and also of 1:1 electrolytes with different radii.

Acknowledgement

We are grateful to Prof. Niels J. Bjerrum, Materials Science Group, Chemical Laboratory A, Technical University of Denmark for his continuous support of the present project.

References

[1] T.S. Sørensen and P. Sloth, "Ion and potential distributions in charged and non-charged primitive spherical pores in equilibrium with primitive electrolyte solution calculated by grand canonical ensemble Monte Carlo simulation: Comparison with generalized Debye-Hückel and Donnan theory", *J. Chem. Soc. Faraday Trans*, **88**, 571 (1992).

[2] S. R. Rivera and T. S. Sørensen, "Grand Canonical Ensemble Monte Carlo simulations of Donnan potentials, nonelectroneutrality, activity coefficients and excess energy in spherical charged or uncharged pores with restricted primitive model electrolytes", *Molecular Simulation*, **13**, 115 (1994).

[3] B. Malmgren-Hansen, T. S. Sørensen, B. Jensen and M. Hennenberg, "Electric impedance of cellulose acetate membranes and a composite membrane at different salt concentrations", *J. Colloid Int. Sci*, **130**, 359 (1989).

[4] T. S. Sørensen, "Ions in solution and in weak ion exchange membranes" in *Capillarity Today. Lecture Notes in Physics, Vol. 386*, G. Pétré and A. Sanfeld, eds., Springer-Verlag, Berlin-Heidelberg-New York- London -Paris-Tokyo-Hong Kong-Barcelona-Budapest, 1991, pp. 164-221.

[5] T. S. Sørensen, B. Malmgren-Hansen and B. Jensen, "Electromotive force and impedance studies of cellulose acetate membranes: Evidence for two binding sites for divalent cations and for an alveolar structure of the skin layer", *Desalination* **80**, 293 (1991).

[6] I. W. Plesner, B. Malmgren-Hansen and T.S. Sørensen, "Distribution of electrolytes between membraneous and bulk phases, and the dielectric properties of membraneous water, studied by impedance spectroscopy measurements on dense cellulose acetate membranes", *J. Chem. Soc. Faraday Trans*, **90**, 2381 (1994).

[7] V. Compañ, M. L. López, T. S. Sørensen, and J. Garrido "Transport numbers in the surface layers of asymmetric membranes from initial time measurements". *J. Phys. Chem.*, **98**, (1994). In press.

[8] P. Sloth and T. S. Sørensen, "Single-ion activity coefficients and structure of ionic fluids. Results for the primitive model of electrolyte solutions", *J. Phys. Chem.*, **94**, 2116 (1990).

[9] T. S. Sørensen, "Error in the Debye-Hückel approximation for dilute primitive model electrolytes with Bjerrum parameters of 2 and ca. 6.8 investigated by Monte Carlo Methods: Excess energy, Helmholtz free energy, heat capacity and Widom activity coefficients corrected for neutralising background", *J. Chem. Soc. Faraday Trans.*, **87**, 479 (1991).

[10] T. S. Sørensen, "High precision canonical ensemble Monte Carlo simulations of very dilute primitive Z:Z and 2:1 electrolytes and of moderately concentrated 1:1 electrolyte mixtures", *Molecular Simulation*, **11**, 1 (1993).

[11] T.S. Sørensen, "Direct calculation of the electric potential distributions around ions from high precision canonical ensemble Monte Carlo simulations of some primitive model electrolyte systems", *Molecular Simulation*, **11**, 267 (1993).

[12] T. M. Reed and K. E. Gubbins, *Applied Statistical Mechanics*, McGraw-Hill, New York, 1973.

[13] L. Onsegar and N. T. Samaras, *J. Chem. Phys.*, **2**, 528 (1934).